Journal of Computational Neuroscience (2019) 46:299–320
https://doi.org/10.1007/s10827-019-00718-4

Neural network model of an amphibian ventilatory central pattern generator

Ginette Horcholle-Bossavit[1,2] · **Brigitte Quenet**[1,2]

Received: 3 July 2017 / Revised: 25 April 2019 / Accepted: 2 May 2019 / Published online: 22 May 2019

Abstract

The neuronal multiunit model presented here is a formal model of the central pattern generator (CPG) of the amphibian ventilatory neural network, inspired by experimental data from *Pelophylax ridibundus*. The kernel of the CPG consists of three pacemakers and two follower neurons (buccal and lung respectively). This kernel is connected to a chain of excitatory and inhibitory neurons organized in loops. Simulations are performed with Izhikevich-type neurons. When driven by the buccal follower, the excitatory neurons transmit and reorganize the follower activity pattern along the chain, and when driven by the lung follower, the excitatory and inhibitory neurons of the chain fire in synchrony. The additive effects of synaptic inputs from the pacemakers on the buccal follower account for (1) the low frequency buccal rhythm, (2) the intra-burst high frequency oscillations, and (3) the episodic lung activity. Chemosensitivity to acidosis is implemented by an increase in the firing frequency of one of the pacemakers. This frequency increase leads to both a decrease in the buccal burst frequency and an increase in the lung episode frequency. The rhythmogenic properties of the model are robust against synaptic noise and pacemaker jitter. To validate the rhythm and pattern genesis of this formal CPG, neurograms were built from simulated motoneuron activity, and compared with experimental neurograms. The basic principles of our model account for several experimental observations, and we suggest that these principles may be generic for amphibian ventilation.

Keywords Ventilatory CPG model · Metamorphosis · Neurogram simulation · Pacemakers · Amphibian

1 Introduction

In amphibians, respiratory gas exchanges occur in several locations (skin, gills and lungs), and the relative contribution of each of these respiratory modes changes with development (Burggren and West 1982). The first developmental stages take place in water, and gas exchange of both O_2 and CO_2 occurs through the skin and the gills (Sundin et al. 2007). With metamorphosis, the animal's metabolic needs increase. The gills regress, and the lungs, which are more efficient for respiratory function, and in particular for oxygen uptake, expand. Elimination of CO_2 becomes the critical factor in the maintenance of internal milieu, and the associated chemosensitivity to acidosis increases (Gargaglioni and Milsom 2007; Sundin et al. 2007). In the aquatic environment, pre-metamorphic tadpoles respire by propelling water over the gills. Rhythmic contractions of the mouth muscles move the buccal floor up and down, causing water to flow over the gills. This buccal pump is activated by a buccal neuronal command. In post-metamorphic tadpoles, the buccal pump also fills and empties the oropharynx with air, but both lung inflation (inspiration) and deflation (expiration) are enabled by coordinated opening of the glottis and closing of the nares, which are activated by a predominant neuronal command, the lung command (Vasilakos et al. 2006). The lung ventilation neuronal command becomes more and more frequent after metamorphosis, while only small oscillations of the buccal floor persist (Burggren and Doyle 1986). Most studies of the amphibian ventilatory neuronal command have examined neurograms recorded from cranial nerves (V, VII,

Action Editor: Frances K. Skinner

Electronic supplementary material The online version of this article (https://doi.org/10.1007/s10827-019-00718-4) contains supplementary material, which is available to authorized users.

✉ Brigitte Quenet
Brigitte.Quenet@espci.fr

[1] Équipe de Statistique Appliquée, ESPCI-Paris, PSL Research University, F-75005 Paris, France

[2] Neurophysiologie respiratoire expérimentale et clinique, INSERM, UMRS1158, Sorbonne Université, F-75005 Paris, France

IX and X) in isolated brainstem preparations of the bullfrog tadpole (*Lithobates catesbeianus*/*Rana catesbeiana*). These preparations exhibit ventilatory motor rhythms similar in frequency to those characterized *in vivo* (Sakakibara 1984a; 1984b; McLean et al. 1995; Torgerson et al. 1997; Gdovin et al. 1998; Wilson et al. 1999; Gdovin et al. 1999). In the neurograms, the buccal rhythm is characterized by periodic bursts while the lung rhythm is expressed as less frequent episodic shorter bursts of higher amplitude. There is some evidence that two separate brainstem respiratory oscillators are involved in rhythm generation, one for the buccal rhythm and another for the lung rhythm (Vasilakos et al. 2006). Spontaneous expression of a functional neuronal lung command is observed in pre-metamorphic tadpoles. Though infrequent while the buccal command is active, its expression becomes more frequent when the buccal command is absent (Galante et al. 1996; Duchcherer et al. 2013). Several studies have explored the central chemosensitivity that influences the buccal rhythms and the frequency of lung episodes. Indeed, the effects of pH changes corresponding to normocapnia ($pH = 7.8$) or hypercapnia ($pH < 7.8$ or acidosis) were assessed in the isolated tadpole brainstem, at different developmental stages (Torgerson et al. 1997; Taylor et al. 2003; Vinaya and Ignatius 2018; Straus et al. 2011). The lung oscillator has a rostral position while the buccal oscillator is located more caudally (Vasilakos et al. 2006; Duchcherer et al. 2013). They likely involve premotor neurons that project onto motoneuron populations innervating respiratory muscles. Optical signals also revealed that ventilatory rhythmic activity was exhibited by a longitudinal column in the ventrolateral medulla between the levels of trigeminal and hypoglossal rootlets (Oku et al. 2008). In mammals, the existence of two respiratory oscillators has been well characterized in rats (for review see Feldman and Del Negro 2006).These are associated with two brainstem nuclei, the pFRG and the preBötC (Smith et al. 1991; Onimaru et al. 2003). It has been hypothetized that these oscillators may have originated from those controlling the gills and lungs of the earliest air breathers (Wilson et al. 1999; Vasilakos et al. 2004) -the frog buccal center is suggested to be analogous to the rat pFRG, and the lung center to the preBötC- though their relative positions along the rostro-caudal axis are reversed. There has been much computational modeling of the fundamental mechanisms of respiratory central pattern generation in mammals, often integrating large amounts of experimental data (see for instance Wittmeier et al. 2008; Rubin et al. 2011; Carroll and Ramirez 2013; Guerrier et al. 2015; Lal et al. 2016; Anderson and Ramirez 2017; Diekman et al. 2017; Molkov et al. 2017). Inspiratory and expiratory phases are clearly separated in mammals, so their CPG models attribute specific neuronal units to these functions, active at precise phases of the ventilatory periodic cycle. In contrast, there have been few computational studies of respiratory rhythm generation in amphibians: the two-oscillator Morris-Lecar neuron network (Bose et al. 2005), and the Izhikevich loop-chain with synchronisation (Horcholle-Bossavit and Quenet 2009). In amphibians, both lung inflation and deflation are governed by the same neuronal episodic lung command superimposed on a basis of a periodic buccal command. The amphibian ventilatory command organization seems to differ essentially from the mammalian, and direct resemblances, however justified from a phylogenetic point of view, are difficult to establish. Our model of the amphibian ventilatory neuronal network is informed by several experimental studies. Galante et al. (1996) recorded neurograms of the in vitro brainstem of the bullfrog tadpole, and showed that gill rhythmicity, expressed earlier in development than lung activity, seems to be dependent on synaptic inhibition. They also suggest that gill rhythmogenesis involves neurons with pacemaker properties. This constitutes an interesting synthetic framework for developing a model able to account for some processes involved in the genesis of the amphibian breathing patterns. Our model is also informed by our earlier study of neurograms from the marsh frog *Pelophylax ridibundus* (Quenet et al. 2014). Our analysis of these neurograms, recorded in pre- and post-metamorphic tadpole brainstem preparations, was based on continuous wavelet transform (CWT), as well as spectral and cross-correlation analyses, and centered on buccal activity. It revealed the internal structure of the buccal bursts. In particular, fast oscillations (20-25 Hz) characterize these bursts and are prominent in pre-metamorphic tadpoles.

We have built the formal neuronal model presented here in order to model the basic mechanisms underlying the complex temporal patterns of global brainstem-spinal amphibian ventilatory network activity. Our ventilatory central pattern generator (CPG) had to incorporate three major experimental facts: (1) buccal and lung activity depends on the tadpole's stage of development (pre- or post-metamorphic); (2) such activity is also dependent on pH; and (3) buccal bursts exhibit intra-burst structured high frequency oscillations. In this network model, the CPG sensitivity to pH is supplied by a neuronal chemosensitivity. The chemoreceptor is modeled as an autonomous regular spiking neuron (Perkel et al. 1964), i.e. a pacemaker neuron, whose firing frequency increases as the pH falls (Rigatto et al. 2000). It sends an excitatory input to two follower neurons representing the two identified command centers, the buccal command center and the lung command center, which integrate information from this input, as well as information from other pacemaker neurons. The network is built with formal neurons of Izhikevich-type (Izhikevich 2003). The CPG is composed of a core of 5 excitatory neurons including 3 pacemakers, and a loop-chain of 70 excitatory and inhibitory neurons, including premotor neurons. The

model was validated by computing simulated neurograms from summed motoneuron activities driven by the premotor neurons. These simulated neurograms were analyzed with the same signal processing tools used for the analysis of experimental neurograms (Quenet et al. 2014).

2 Method

Our complete network consists of two functionally distinct groups of connected Izhikevich-type formal neurons: a CPG and a motoneuron layer. The main part of the model, with its dynamic properties, resides in the CPG, a recurrent network that projects inputs through a feedforward pathway to the motoneuron layer. The CPG network is built with pacemaker neurons, excitatory follower neurons, and excitatory and inhibitory chain neurons. The only role of the motoneuron layer is to constitute a neuronal access to the CPG output in order to mimic the physiological conditions in which neurograms are elaborated.

2.1 Izhikevich type neuron

The standard Izhikevich neuron captures many biological properties of realistic Hodgkin-Huxley type conductance-based models, with a simpler numerical implementation (Izhikevich 2003; 2004). In this model, the potential of each neuron is given by the two ordinary differential equations in Eq. (1):

$$\begin{aligned} \frac{dv_i}{dt} &= 0.04 \cdot v_i^2 + 5 \cdot v_i + 140 - u_i + I_i \\ \frac{du_i}{dt} &= a \cdot (b \cdot v_i - u_i) \end{aligned} \tag{1}$$

The equations in Eq. (1) are implemented on the basis of an explicit first-order Euler scheme, using the stabilising leapfrog method: at each time step, $v_i(t)$ is computed using $v_i(t - dt)$ and $u_i(t - dt)$, but $u_i(t)$ is computed using $v_i(t)$ rather than $v_i(t-dt)$. The integration time step dt represents a biological time duration of 1 ms when it equals 1; in the simulations of the present neural network model, $dt = \frac{1}{8}$ ms, $v_i(t)$ is the membrane potential in mV of neuron i at time t, and $u_i(t)$, in mV, is an auxiliary negative feedback variable at time t. The two dimensionless parameters a and b define the neuron type, together with two other parameters c and d, introduced for resetting $v_i(t)$ and $u_i(t)$, respectively (see Eq. (2) below). In this situation, the state of neuron i at time t is $S_i(t)$, which equals 1 when $v_i(t) \geq 30$ mV (spike emission) and otherwise equals 0. The after-spike resetting is defined by the following conditions:

$$\begin{aligned} v_i &\leftarrow c \\ u_i &\leftarrow u_i + d \end{aligned} \tag{2}$$

The parameter values a and b are standard values for the tonic spiking Izhikevich Model. The d parameter of the pacemaker neurons is not critical, since, whatever d, the input currents can be adapted to get the target frequencies. However, the d value for the two followers is lower than the others, in order to get a greater sensitivity to the synaptic input current. All these parameter values are given in Table 1.

A modification of the standard Izhikevich neuron is introduced as a constraint on the value of $v_i(t)$ before computing $u_i(t)$: it introduces an explicit refractory period which limits the spiking frequency of neuron i. Once the differential equations in Eq. (1) are implemented, $v_i(t)$ may be computed:

$$\begin{aligned} v_i(t) &= v_i(t - dt) + dt \cdot (0.04 \cdot v_i(t - dt)^2 + 5 \cdot v_i(t - dt) \\ &= +140 - u_i(t - dt) + I_i(t)) \end{aligned} \tag{3}$$

If $v_i(t)$ is higher than a reference membrane potential value (-55 mV), and the time delay from the last spike of neuron i is smaller than a given refractory period (1.5 ms), a correction of (-2 mV) is applied to $v_i(t)$ before the computation of $u_i(t)$:

$$\begin{aligned} v_i(t) &= (v_i(t) - 2) \\ u_i(t) &= u_i(t - dt) + dt \cdot (a \cdot (b \cdot v_i(t) - u_i(t - dt))) \end{aligned} \tag{4}$$

The input and synaptic contributions to Izhikevich neuron i at time t are delivered through the variable $I_i(t)$ in mV (cf. Eq. (3)), which represents an input current in mA multiplied by an implicit resistance of 1 ohm. It is made up of three contributions: an 'extrinsic' current $I_i^{ext}(t)$, related to the external contributions as detailed below, an 'intrinsic' current or membrane current I_i^{memb}, accounting

Table 1 Values of a, b, c and d for the different types of neurons

where	type	a	b	c	d
Pre-metamorphic					
CPG	Pacemakers	0.02	0.2	−65	5
CPG	Followers	0.02	0.2	−65	0.02
CPG	Excit/Inhib	0.02	0.2	−65	1.5
Mot	MN1	0.02	0.2	−80	3
Mot	MN2	0.02	0.2	−80	8
Post-metamorphic					
CPG	Pacemakers	0.02	0.2	−65	5
CPG	Followers	0.02	0.2	−58	0.001
CPG	Excit/Inhib	0.02	0.2	−65	0.1
Mot	MN1	0.02	0.2	−80	0.05
Mot	MN2	0.02	0.2	−80	0.2
Mot	MN3	0.02	0.2	−80	0.1

for membrane properties, and a stochastic noise current $I_i^{stoch}(t)$:

$$\begin{aligned} I_i(t) &= I_i^{ext}(t) + I_i^{memb} + I_i^{stoch}(t) \\ I_i^{stoch}(t) &\sim \mathcal{N}(0, \sigma^2) \end{aligned} \tag{5}$$

The value of dt has been chosen as a negative power of 2, in order to code it exactly according to IEEE floating point format. We have verified that with dt lower than or equal to 2^{-3}, the network spiking pattern is stable. Our simulations were done with $dt = 2^{-3}$ for computational efficiency. The noise current applied to neuron i at time t is $I_i^{stoch}(t)$, a stochastic realisation of a pseudo-random generator, independently of all other realisations. It is supposed to correspond to small fluctuations of the synaptic currents, without big jumps, which is described adequately by a Gaussian white noise (Vinaya and Ignatius 2018). $\mathcal{N}(0, \sigma^2)$ is a centered normal distribution with standard deviation σ. In the CPG simulations, σ is set at 0.2 and is increased for the noise robustness analysis.

2.2 Synaptic contributions

We consider synapses as sources of current and not conductances *stricto sensu*, i.e., the synaptic current does not depend on the postsynaptic membrane potential (Roth and Van Rossum 2009). The current contribution $I_i^{ext}(t)$ on neuron i at time t is computed:

$$I_i^{ext}(t) = \sum_{j=1}^{N} I_{ij}^{syn}(t) + I_i^{add}(t) \tag{6}$$

where $I_{ij}^{syn}(t)$ is the explicit synaptic current from presynaptic neuron j to postsynaptic neuron i in a network of N neurons, and $I_i^{add}(t)$ is an additional diffuse 'synaptic' current that concerns the motoneuron layer only. The synaptic current $I_{ij}^{syn}(t)$ is either excitatory, $I_{ij}^{syn-ex}(t)$, or inhibitory, $I_{ij}^{syn-in}(t)$. Both are of instantaneous rise/single-exponential decay type (Roth and Van Rossum 2009). The analytical expression of the exponential synapse decay for $t > t_0$, when the synaptic rise occurred at t_0, is given by the corresponding recurrent equation:

$$\begin{aligned} I_{ij}^{syn}(t_0) &= w_{ij} \cdot G_{\max} \\ I_{ij}^{syn}(t) &= w_{ij} \cdot G_{\max} \cdot e^{-\delta \cdot (t - t_0)} \\ \Rightarrow I_{ij}^{syn}(t) &= I_{ij}^{syn}(t - dt) \cdot (1 - \delta \cdot dt) \\ t &> t_0 \end{aligned} \tag{7}$$

where w_{ij} is the weight of the synapse from neuron j to neuron i, which is positive for an excitation or negative for an inhibition, $G_{\max}$ is the maximal current of a synapse of weight equal to 1, and δ is the rate of the synapse exponential decay. The excitatory explicit synaptic current is computed for $I_{ij}^{syn-ex}(t)$:

$$\begin{aligned} I_{ij}^{syn-ex}(t) &= w_{ij} \cdot G_{\max}^{ex} \cdot S_j(t - \tau) \\ &\quad + I_{ij}^{syn-ex}(t - dt) \cdot (1 - \delta^{ex}.dt) \\ w_{ij} &> 0 \end{aligned} \tag{8}$$

where $G_{\max}^{ex}$ is the maximal current of an excitatory synapse of weight equal to 1, δ^{ex} is the rate decay for an excitatory synapse, and τ is the transmission delay, $\frac{1}{8}$ ms (equal to dt) for all synapses. The inhibitory explicit synaptic current is computed for $I_{ij}^{syn-in}(t)$:

$$\begin{aligned} I_{ij}^{syn-in}(t) &= w_{ij} \cdot G_{\max}^{in} \cdot S_j(t - \tau) \\ &= + I_{ij}^{syn-in}(t - dt) \cdot (1 - \delta^{in} \cdot dt) \cdot \epsilon_{ij}(t) \cdot \delta^{in} \cdot dt \\ \text{with :} & \\ \epsilon_{ij}(t) &= \alpha \cdot w_{ij} \cdot G_{\max}^{in} \cdot S_j(t - \tau) \\ &\quad + \epsilon_{ij}(t - dt) \cdot (1 - \eta \cdot dt) \\ &= w_{ij} < 0 \end{aligned} \tag{9}$$

Where Ginmax is the maximal current, in absolute value, of an inhibitory synapse of weight equal to (-1), and δ^{in} is the rate decay for an inhibitory synapse. The variable $\epsilon_{ij}(t)$ guarantees that the postsynaptic neuron i membrane potential remains inferior or equal to the resting potential after any effective inhibition. It is computed with two factors, $\alpha = 0.05$, and $\eta = 0.01$. This correction is applied to avoid artifactual post-inhibitory spiking. The synaptic parameters have been adapted in order to get the target neuronal dynamics and their values are given in Table 2.

2.3 Core of the CPG: Pacemakers and additive synaptic effect on followers

Pacemaker neurons are defined as autonomous regular firing neurons (Wittmeier et al. 2008). Each pacemaker neuron i is implemented as a neuron receiving a steady (or periodic) depolarizing current $I_i^{memb} = I_i^P$ whose intensity (or frequency) determines the pacemaker frequency. When

Table 2 Values of $G_{\max}$ and δ for the different types of synapses

where	type	$G_{\max}$[mV]	δ [ms^{-1}]
Pre-metamorphic			
CPG	Synexcpg	48	0.19
CPG	Synincpg	10	0.05
Mot	Synexmot	2.5	0.05
Post-metamorphic			
CPG	Synexcpg	48	0.19
CPG	Synincpg	10	0.05
Mot	Synexmot	50	8.9

a follower $F1$ receives synaptic excitatory inputs from two pacemakers $P1$ and $P2$ firing at frequencies $\nu 1$ and $\nu 2$ respectively, its membrane potential performs an addition of the corresponding synaptic potentials. The spikes of $P1$ and $P2$ are periodically coincident at frequency $|\nu 1 - \nu 2|$, so the follower membrane potential oscillates at this frequency too, with a maximum corresponding to the periods when the pacemaker spikes are the most coincident. With adapted synaptic weights, when $P1$ and $P2$ are spiking almost in phase, $F1$ exhibits a spiking activity, and is otherwise silent. The burst frequency of $F1$ corresponds to $|\nu 1 - \nu 2|$ and the intra-burst frequency is around $\frac{\nu 1+\nu 2}{2}$. Depending on the synaptic weights, this additive synaptic effect at the level of the post-synaptic follower membrane may lead, for each higher value of the membrane potential modulation, to one or more spikes. Thus, the follower firing pattern may exhibit two frequencies: the burst low frequency and the high spiking frequency inside the bursts. In Fig. 1a, $F1$ receives synaptic excitatory inputs with the same synaptic weights from two pacemakers $P1$ and $P2$. In Fig. 1b, a follower $F2$ receives synaptic excitatory inputs from three pacemakers $P1$, $P2$, and $P3$, whose frequencies are $\nu 1$, $\nu 2$, and $\nu 3$, respectively. The synaptic weights from $P2$ and $P3$ are equal, set at a value too weak to elicit any spiking activity. However, the additive effect between $P2$ and $P3$ modulates $F2$ membrane potential at the frequency $|\nu 2 - \nu 3|$ in such a way that a small increase due to the synaptic effect from pacemaker $P1$, when coincident with the two other pacemakers, may elicit a spike, or not, leading to episodic spiking activity of $F2$. In Fig. 1c, two followers, $F1$ and $F2$, receive synaptic excitatory inputs from three pacemakers $P1$, $P2$, and $P3$. $P1$ and $P3$ are the dominant pacemakers

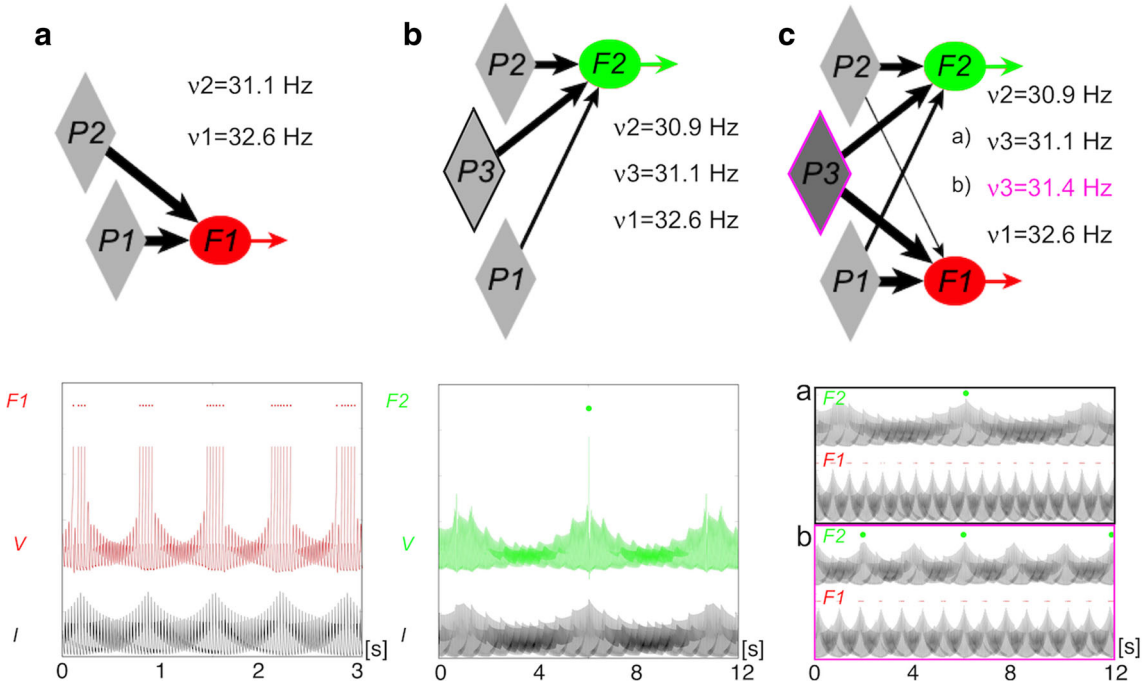

Fig. 1 Periodic modulations of the follower membrane potentials. **a** The buccal follower $F1$ receives excitatory inputs from Pacemakers $P1$ and $P2$. $F1$ membrane potential and spikes are shown in red line and red dots, respectively and the corresponding synaptic input current from $P1$ and $P2$ is shown in black traces, revealing the periods when $P1$ and $P2$ spike in phase and the periods when they spike in anti-phase. When $P1$ and $P2$ are spiking in phase, $F1$ exhibits a spiking activity, and it is silent otherwise. The burst frequency of $F1$ corresponds to the difference between the frequencies of $P1$ and $P2$ (32.6 Hz-31.1 Hz = 1.5 Hz). **b** The lung follower $F2$ receives excitatory inputs from the three pacemakers $P1$, $P2$ and $P3$. $P2$ and $P3$ are connected to $F2$ with strong synapses (thick arrows) and $P1$ is connected to $F2$ with a weak synapse (thin arrow). $F2$ membrane potential and spike are shown in green line and green dot, respectively, and the corresponding synaptic input current from $P1$, $P2$ and $P3$ is shown in black traces. In this case, the membrane threshold for spiking is reached only once during three periods of the membrane modulation, modulation that reflects the periodic modulation of the synaptic input current, whose dominant frequency corresponds to the difference between the frequencies of $P3$ and $P2$ (31.1 Hz-30.9 Hz = 0.2 Hz). The unique spike results from the spike coincidence of the three presynaptic pacemakers. **c** The three pacemakers $P1$, $P2$ and $P3$ are connected to the two followers: the buccal periodic bursting follower $F1$ and the lung episodic spiking follower $F2$. The connections $P1 \mapsto F1$ and $P3 \mapsto F1$ are dominant for $F1$ (thick arrows), while the dominant connections to $F2$ are $P2 \mapsto F2$ and $P3 \mapsto F2$. The frequencies of $P1$ and $P2$ are fixed, while the frequency of $P3$, the equivalent of a chemosensitive pacemaker, is increased with 'hypercapnia' (i.e when the pH changes from 7.8 to 7.4) from 31.1 Hz to 31.4 Hz (magenta). This frequency increase of $P3$ induces two effects on the follower activities (from a) to b)): a decrease of the periodic bursting frequency of the buccal follower $F1$ (from 1.5 Hz to 1.2 Hz) and an increase of the periodic modulation of the synaptic input to $F2$ (from 0.2 Hz to 0.5 Hz), thus, consequently, an increase in the number of spiking occurrences of the episodic lung follower $F2$ (green dots)

on $F1$, with synaptic weights leading $F1$ to exhibit a cyclic bursting activity; the synaptic efficiency of the connection from $P2$ to $F1$ is low, introducing some irregularities. $P2$ and $P3$ are dominant pacemakers on $F2$, and together with the low synaptic efficiency connection from $P1$ to $F2$, they elicit an episodic response from $F2$. When the frequency of $P3$ -which is dominant on both followers- is increased, the burst frequency of $F1$ decreases while the frequency of the membrane potential modulation of $F2$ increases (compare Fig. 1cb, where the burst frequency of $F1$ is 1.2 Hz, and there are three $F2$ spikes, with Fig. 1ca, where the burst frequency of $F1$ is 1.5 Hz, and there is only one $F2$ spike). This means that increasing the frequency of $P3$, which represents a chemosensitive pacemaker, may induce simultaneously two opposite effects on $F1$ and $F2$: a decrease in the bursting frequency of $F1$ and an increase in the episodic firing frequency of $F2$ (because its firing possibility increases, which is due to the increased membrane potential oscillation frequency, whose maxima are more frequently close to the spiking threshold).

2.4 Central pattern generator network

The architecture of the CPG, illustrated in Fig. 2a, is based on two components. The first component is a generator core of 5 neurons (3 pacemakers and 2 followers), with the same configuration described above in Section 2.3 and illustrated in Fig. 1c. The periodic follower $F1$ is now B, the buccal follower. The episodic follower $F2$ is now L, the lung follower. Pacemaker $P1$ is now BP, i.e. a dominant pacemaker for B, while pacemaker $P2$ is now LP, a dominant pacemaker for L. Pacemaker $P3$ is now CH, dominant for both B and L. It represents the chemosensitive element of the network, whose regular firing frequency increases as the pH falls from 7.8 to 7.4. CO_2-chemosensitive neurons have been observed to display such increases in frequency in several empirical studies (Ballantyne and Scheid 2000; Putnam et al. 2004; Santin and Hartzler 2013; Rigatto et al. 2000).

The second component of the CPG network is a set of connected loops organized in a chain whose basic loop is shown in Fig. 2b. From an anatomical point of view, we consider a rostro-caudal extension of the chain as suggested by optical recordings (Oku et al. 2008). The core is connected with the chain as follows: the B follower, which is neuron n°1 of the network, is an excitatory presynaptic neuron to the first neuron of the chain (neuron n°2), and is inhibited by the first inhibitory neuron(s) of the chain (neuron n°3 for pre-metamorphic tadpoles, and neurons n°3, 5, and 7 for post-metamorphic tadpoles). The L follower (neuron n°75) is an excitatory presynaptic neuron to all the neurons of the chain and it is inhibited by all the inhibitory neurons of the chain. When B follower is active, each excitatory neuron of the chain transmits a delayed copy of the periodic activity of B. This delay corresponds to the sum of conduction and synaptic transmission times (included in the synaptic delay τ) and the membrane integration time until spiking. The activity pattern of the followers depends on the balance between the excitatory contributions from the pacemakers and the inhibitory contributions from the chain inhibitory neurons, when active. Fig. 2c illustrates part of the CPG chain, together with six excitatory neurons (n°50, 52, 54, 56, 58, 60) which form a 'premotor module' that projects excitatory synapses onto motoneuron population(s). The matlab simulation codes is made available through ModelDB

2.5 Motoneuron layer and simulated neurograms

There are two motoneuron subpopulations, $MN1$ and $MN2$ for the pre- and post-metamorphic stages, and, additionally, a third, $MN3$ is specific to the post-metamorphic stage. In subpopulations $MN2$ and $MN3$ -comprised of N^{mn2} and N^{mn3} neurons respectively- the generic element m receives an excitatory synaptic current from the N^{cpg} premotor neurons: $\sum_{j=1}^{N^{cpg}} I_j^{syn}(t)$ that is independent of m (see Fig. 2c). All of these neurons also receive the same additional current $I^{add}(t)$ representing the global modulation effects of weak and diffuse synaptic implicit contacts from excitatory and inhibitory neurons of the CPG in the neighborhood of the 'premotor module' (all neurons from n°40 to n°70). The other subpopulation, $MN1$-comprised of N^{mn1} neurons- has no explicit synaptic connection from the CPG, but is activated by the CPG through the modulation current $I^{add}(t)$ only. All the $N^{mot} = N^{mn1}+N^{mn2}$ (+ N^{mn3} in the post-metamorphic stage) receive the noise current $I_m^{stoch}(t)$. The various contributions to the global current $I_m(t)$ received by a motoneuron m of a subpopulation are expressed as follows:

$$\begin{aligned} I_m(t) &= I^{add}(t) + I_m^{memb} + I_m^{stoch}(t) \\ &\quad \forall m \in MN1 \\ I_m(t) &= \sum_{j=1}^{N^{cpg}} I_j^{syn}(t) + I^{add}(t) + I_m^{memb} + I_m^{stoch}(t) \\ &\quad \forall m \in MN2 \end{aligned} \tag{10}$$

The current I_m^{memb}, which defines the membrane threshold of motoneuron m, is distributed according to the same function illustrated in (11) for the three populations; N represents N^{mn1}, N^{mn2} or N^{mn3}, and I^{off} , β and γ are different for the different populations.

$$I_m^{memb} = I^{off} - \frac{1}{\beta} \cdot \left(ln(\frac{((m-1) \cdot e^{\beta \cdot \gamma} - 1)}{N-1} + 1 \right) \tag{11}$$

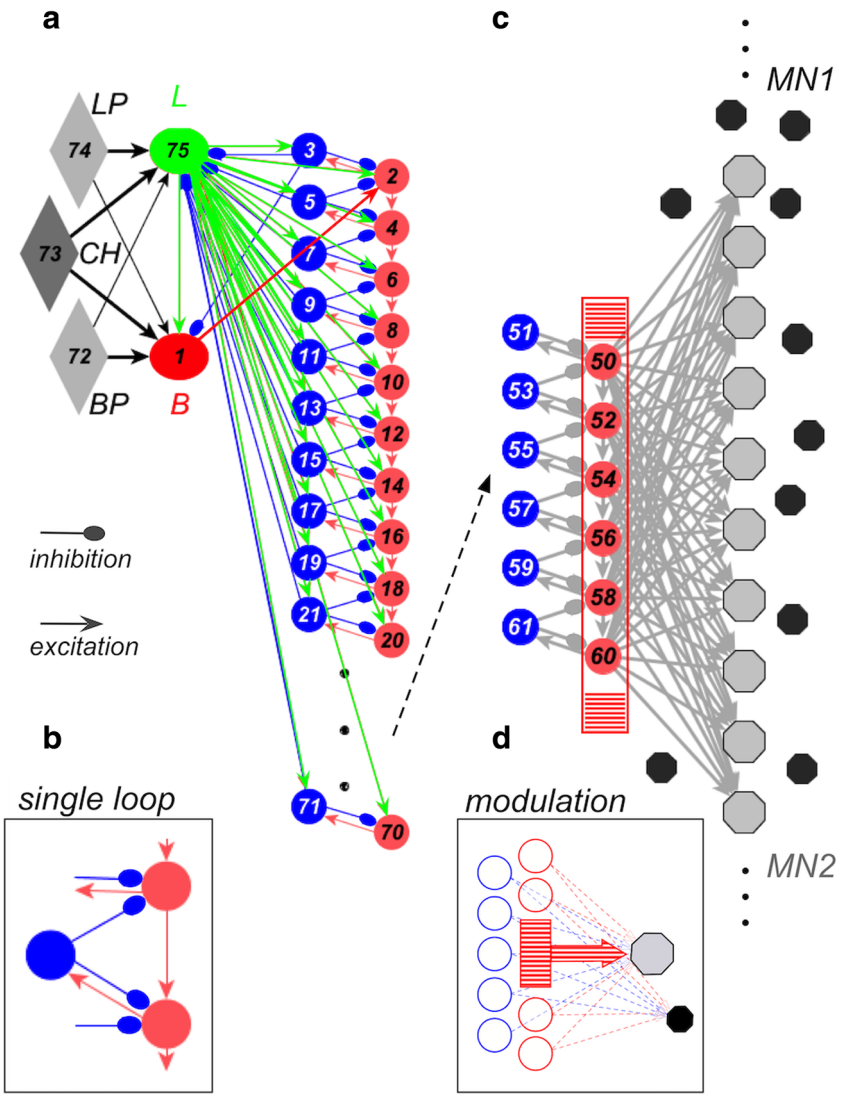

Fig. 2 Architecture of the ventilatory model. **a** Topological configuration of the CPG network with a core of three pacemakers (BP, corresponding to $P1$, LP, corresponding to $P2$, and CH, a 'chemosensitive' pacemaker, corresponding to $P3$ of Fig. 1) and two followers (B, corresponding to $F1$, and L, corresponding to $F2$ of Fig. 1), with a chain composed of loops of connected excitatory and inhibitory neurons. B follower is excitatory to neuron n°2 and receives inhibitory connections from neuron n°3. L follower is excitatory to B and to all the neurons of the chain; it receives inhibition from all inhibitory neurons. **b** Each loop of the chain connects two excitatory neurons and one inhibitory neuron together. The complete CPG comprises 75 neurons. **c** Motoneuron layer and connections from the CPG: six excitatory neurons of the CPG chain (the even numbered neurons from n°50 to 60) are the excitatory premotor neurons projecting onto a single motoneuron subpopulation $MN2$ (gray octagons). Each motoneuron of subpopulation $MN2$ receives excitatory synapses from the six premotor neurons, as illustrated for 10 such motoneurons. There is another motoneuron subpopulation $MN1$ (black octagons), which does not receive any explicit synaptic connection from the CPG, but integrates a modulation current as a smoothed summation of CPG neuron activity around the 6 premotor neurons. The $MN2$ neurons also receive this modulation current. **d** Representation of both the explicit synaptic connection and the diffuse implicit connection between the CPG and the motoneuron layer: the red rectangle and the thick red arrow represent the explicit synaptic connections from the premotor neurons toward $MN2$, and the thin dashed blue and red arrows directed towards $MN1$ and $MN2$ represent the diffuse connection, which drives motoneuron activity through the modulation current

Once the I_m^{memb} for each neuron of a motoneuron subpopulation has been defined, it is possible to compute the number N^{rec} of recruited neurons as a function of a steady current I^{st} applied to the motoneurons. Because I_m^{memb} is a negative monotonic decreasing function of m, if a neuron numbered m is recruited with input current I^{st}, it implies that the neurons numbered from 1 to $m-1$ are also active when they receive I^{st}. In order to measure the minimal current necessary to recruit each single motoneuron m, simulations were performed where the motoneuron receives both its hyperpolarizing membrane current I_m^{memb}, and a steady current I^{st}, which is incremented in order to find the minimal value that allows the motoneuron m to fire with a spike 'train' (at least two spikes). This minimal value

defines the current threshold I_m^{thresh} for motoneuron m. So for each given value of a steady current I^{st}, the number of active neurons N^{rec}, i.e. the number of neurons whose $I_m^{thresh} \leq I^{st}$, is defined as follows:

$$N^{rec}(I^{st}) = \sum_{n=1}^{N} H(I^{st} - I_n^{thresh}) \quad (12)$$

where H is the Heaviside function.

The steps involved in the construction of a simulated neurogram are illustrated in Fig. 3, taking into account that extracellular time course recordings are related to the time course of the first derivative of the membrane potential (Anastassiou et al. 2015; Plonsey 1977). A weighted sum of the derivatives of all motoneurons' membrane potentials is performed, with weights randomly chosen in the interval [-1,1] to account for the amplitude effect of the distribution of distances between axons and the 'recording electrode' (Fig. 3b). A low-filtering post-treatment of this signal is applied in order to allow a visual comparison with the experimental neurograms. Neurograms were simulated for a duration of five minutes, with parameters adapted to obtain 'pre-metamorphic' and 'post-metamorphic' signals, at both $pH = 7.8$ and $pH = 7.4$. From each simulated neurogram, a new signal, S_{10}, is computed as the result of a zero-phase filtering of the neurogram, using a moving average rectangular window of 10 ms width. An additional signal S_{100} is computed in a similar manner, with a window of 100 ms width. The detection of the local minima of S_{100} signal allows the segmentation of S_{10} into cycles (buccal bursts). S_{10} signals are analyzed with the same tools applied to the experimental signals in order to obtain amplitude profiles, through correlation analysis, and frequency profiles, using CWT (Quenet et al. 2014).

3 Results

Simulations of the activities of the CPG neurons and of the motoneurons were performed in two conditions corresponding to both $pH = 7.8$ (normocapnia) and $pH = 7.4$ (hypercapnia or acidosis). The $pH = 7.4$ condition is simulated by an increase in the CH frequency response at the level of the CPG neurons for both pre-metamorphic and post-metamorphic tadpoles. The post-metamorphic stage is based on the same network architecture as the pre-metamorphic network. The activity of the premotor neurons of the CPG chain drives the motoneurons whose global activity leads to the simulated neurograms. The neuronal and synaptic characteristics of the CPG and of the motoneurons are adapted in order to reproduce by simulation the main features observed in the experimental neurograms recorded in brainstem preparations from *Pelophylax ridibundus* tadpoles.

3.1 Pre-metamorphic stage

At the pre-metamorphic stage CPG activity is driven by the buccal follower activity while the lung follower is silent. The buccal activity is characterized by bursts occurring at low frequency (LF) and intra-burst oscillations at high frequency (HF). These characteristics are stably maintained in the presence of synaptic noise.

3.1.1 Activity of the CPG

In the example of CPG activity shown in Fig. 4, the values of the buccal frequencies are those measured in tadpole T2 analyzed in Quenet et al. (2014). Mean BP frequency is set to 32.7 Hz, and mean CH frequency to 31.2 Hz for $pH = 7.8$ and to 31.5 Hz for $pH = 7.4$. Thus, the buccal frequency, i.e., the difference between BP and CH frequencies, appears at 1.5 Hz for $pH = 7.8$ and at 1.2 Hz for $pH = 7.4$, respectively. The weights of the excitatory synapses from BP and CH to the buccal B follower are the main factors which determine the duration of the follower activity, and thus the buccal burst duration. The inhibition received by neuron B from the first inhibitory neuron of the chain (neuron n°3) modulates the intraburst frequency, at values slightly lower than the pacemaker frequencies. This B activity pattern propagates along the chain with a time delay at each transmission. The intra-burst oscillation pattern is modified at each step of the chain by a membrane filtering effect: as the distance from the follower increases, this pattern becomes more regular. The values of the d parameter of the B follower, and of the chain neurons are set so as to obtain, at the level of the 6 excitatory premotor neurons (50, 52, 54, 56, 58 and 60), a quasi-regular activity at the experimentally-observed frequency (around 21 Hz).

3.1.2 Robustness of the CPG activity against noise

The simulation illustrated in Fig. 4 was computed using noise currents whose generic term, $I_i^{stoch}(t)$, is randomly drawn at each time step, and for each neuron. The noise current $I_i^{stoch}(t)$ is a realisation of the zero-centered Gaussian distribution, whose standard deviation σ is put at the value 0.2 in the standard simulations. This noise current represents a physiological synaptic noise that disturbs the original -deterministic- input currents. The effect of this noise current on the neuronal dynamics is evaluated by the computation of a noise ratio, defined as the ratio of the mean noise current absolute amplitude (computed on all the neurons and all the time steps of the simulation) to the mean

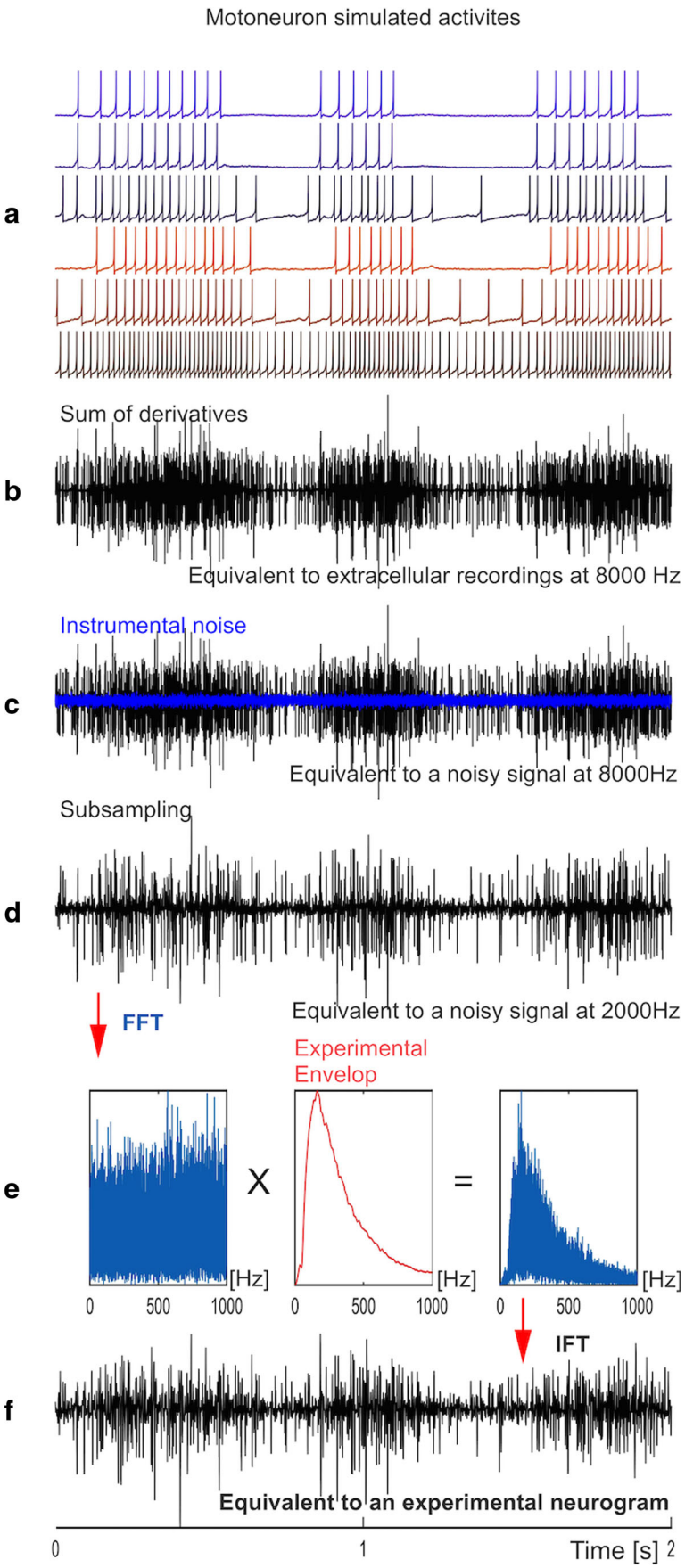

Fig. 3 Step by step building of a simulated neurogram in order to obtain a signal comparable to an experimental neurogram: **a** Membrane potential of three $MN1$ motoneurons (brown, at bottom) and three $MN2$ motoneurons (purple, at top), equivalent to intra-cellular recordings. **b** Random weighted sum of the derivatives of all of the motoneurons' membrane potentials, in order to obtain the equivalent of multiunit extracellular recordings. **c** Addition of a white Gaussian 'instrumental noise' (blue trace) that perturbs the signal by about 12%. **d** Subsampling from 8 kHz (simulation sample rate) to 2 kHz (experimental sample rate for data of *Pelophylax ridibundus*. E) Left: amplitude spectrum computed by Fast Fourier Transform of the subsampled simulated signal over a five-minute period. Center: mean envelope extracted from the amplitude spectrum computed on experimental neurograms. Right: modified amplitude spectrum resulting from the multiplication of the original spectrum of the subsampled simulated signal with the 'experimental envelop'. F) Reconstruction of the simulated neurogram by Inverse Fourier Transform applied to the modified spectrum. By this stage, a simulated neurogram can be compared to an experimental one

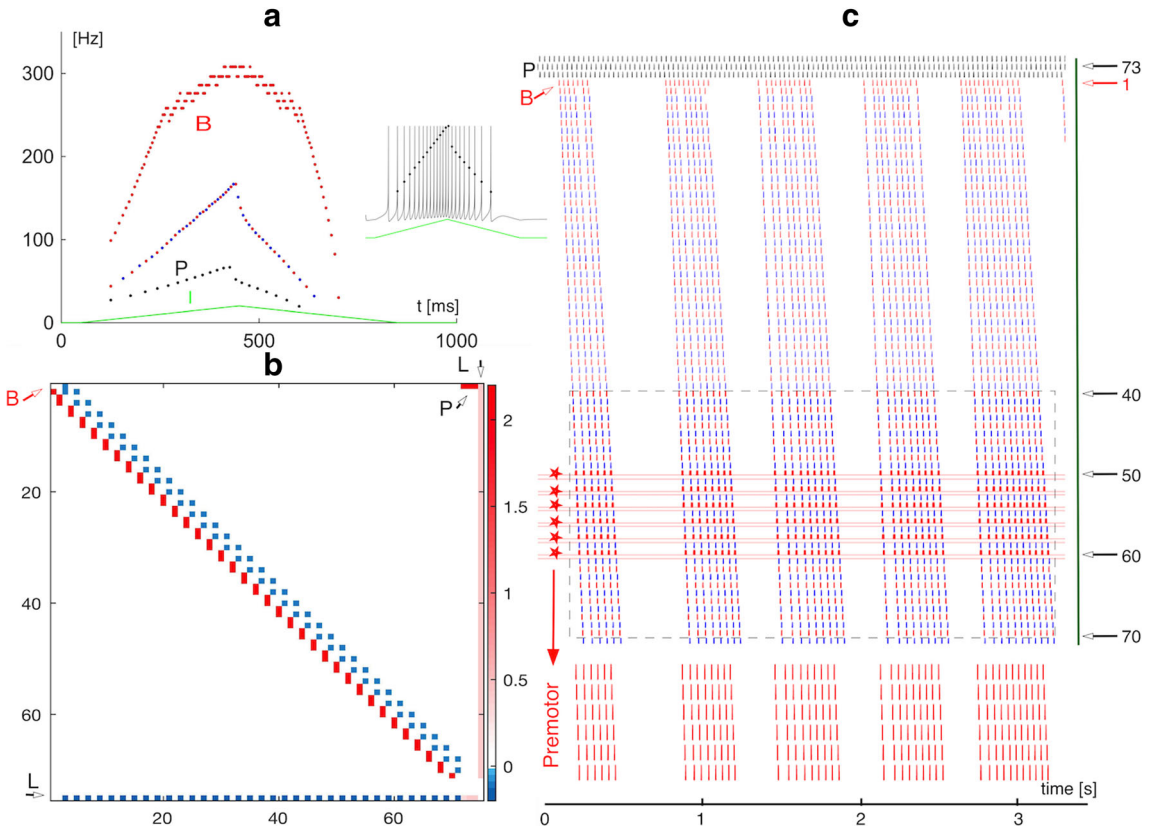

Fig. 4 Neuronal components, connectivity matrix, and activity of the ventilatory pre-metamorphic CPG neurons. **a** The inset shows a neuron membrane potential and its corresponding spiking frequency in response to the up-down ramp current: each dot corresponds to an action potential. Frequency up-down ramp current curves for the three types of CPG neurons (the maximum of the double ramp current I in green is set at a value which corresponds to an external depolarization of 20 mV for all neurons): P for the pacemakers (black dots), B for the buccal follower (red dots), and the other excitatory (red dots) and inhibitory (blue dots) neurons of the chain. **b** Connection matrix of the CPG network as illustrated in Fig. 3: blue squares are inhibitory connections and dark and light red squares are excitatory connections. **c** Raster plot representing 3.5 seconds of CPG neuronal activity at $pH = 7.8$. Six excitatory premotor neurons (the even-numbered neurons from n°50 to 60, indicated by an asterisk) are directly connected to the $MN2$ motoneurons. They are surrounded by 10 preceding neurons (5 excitatory and 5 inhibitory neurons from neuron n°40) and 10 following neurons (5 excitatory and 5 inhibitory neurons, to neuron n°70): they together define a neuronal population (blue dashed rectangle in **c**) which contributes to the motoneuron activity of $MN1$ and $MN2$ through the modulation current. A scatter plot of the activity of the premotor neurons alone is shown below

deterministic current amplitude the neurons receive, in percent. When σ=0.2, for $dt = 2^{-3}$, the noise ratio is about 3% .The noise current is applied to all the 75 neurons of the CPG, including the pacemakers which consequently exhibit jittered regular spiking around their mean frequencies. The value of $\sigma = 0.2$, and its consequence of an about 3% noise ratio, induces a pacemaker jitter that can be estimated by the standard deviation of the pacemaker instantaneous frequency distribution, around 0.15 Hz.

In order to evaluate the robustness of the neuronal CPG model against noise, we performed simulations for a tadpole in normocapnia, for different values of σ within the range $[0 - 4.3]$. The noise ratio quantifies the effect of σ on the neuronal dynamics and the quantification of the effect on the frequency properties of this noisy dynamics is made by using the peak amplitude and frequency at LF and at HF as descriptors, as measured on the frequency profile. The frequency profile is computed with the time frequency map (CWT) of the filtered sum of the membrane potential of the 6 premotor neurons. The red dotted curves of Fig. 5b and c show a slow and regular decrease in the LF peak amplitude (B) with a stable frequency value (C). The black dotted curves of Fig. 5b and c show a slow and regular increase in the HF peak amplitude (B) and a very slow decrease of its frequency value (C). These curves, together with the premotor signals and profiles as illustrated in Fig. 5d, e and f, show that the main features of the CPG activity, the ones that we consider physiologically significant, are present for a wide range of σ, between $[0 - 1.7]$, corresponding to noise ratios up to at least around 30%. In this last case, a pacemaker jitter is about 1.5 Hz. Table 3 indicates, for a tadpole in normocapnia configuration of the network and for $dt = 2^{-3}$ ms, the correspondence between five values of sigma and the noise ratio.

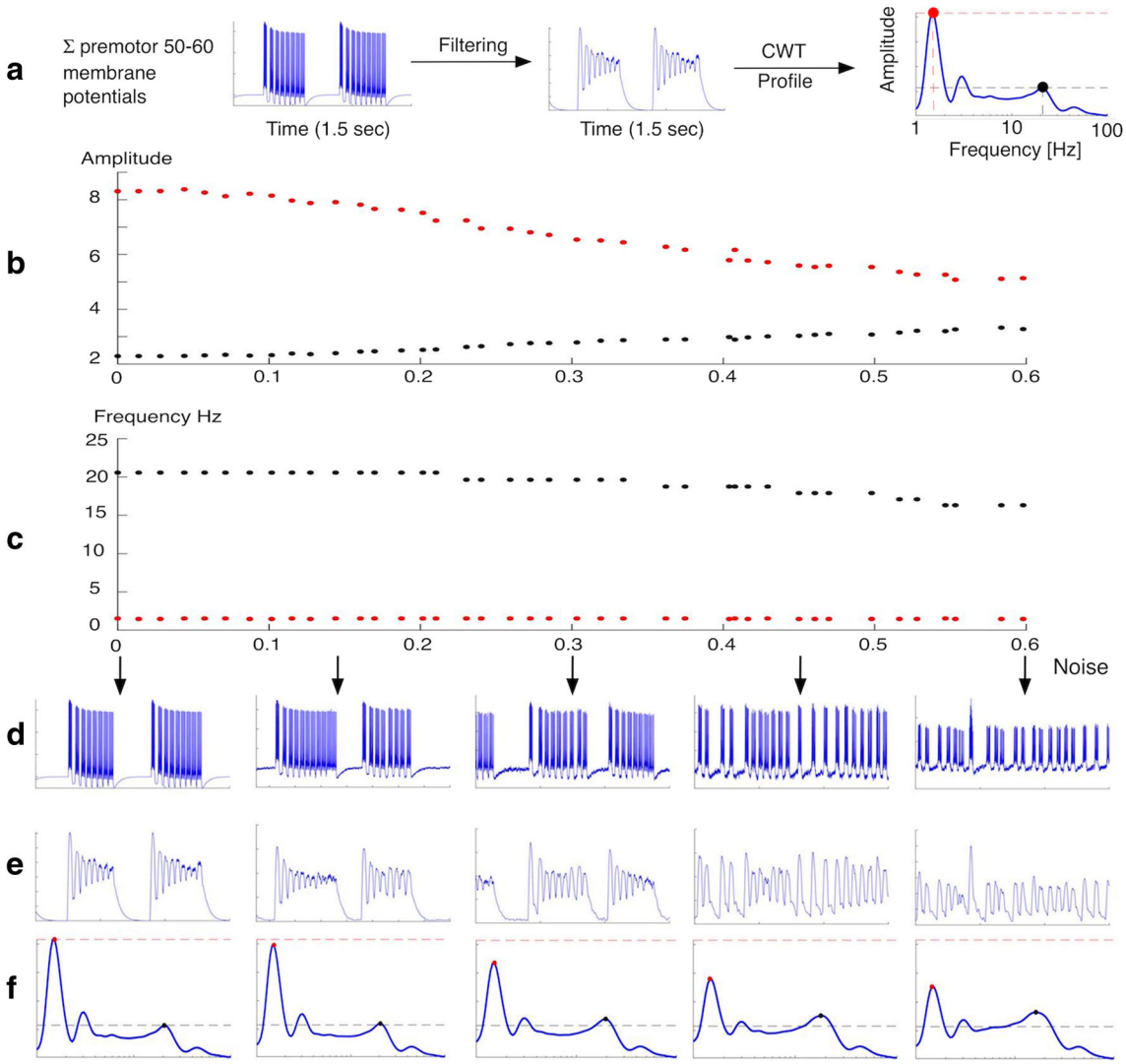

Fig. 5 Effect of synaptic noise on the oscillation pattern and frequency profile at the premotor level. The network corresponds to a tadpole in normocapnia configuration. **a** The sum of the membrane potentials of the premotor neurons (n°50 to 60) is low-pass filtered: this signal exhibits the oscillation pattern of the bursts. The last curve is the corresponding frequency profile. The red and black dots indicate the amplitude of the LF and HF peaks respectively. **b** Evolution of LF (red dots) and HF (black dots) peak amplitudes as functions of the measured noise ratio. **c** Evolution of LF (red dots) and HF (black dots) frequencies as functions of the noise ratio. **d** Sum of the membrane potentials for five values of the noise ratio (0, 15, 30, 45 and 60%) with their corresponding filtered signals (E) and frequency profiles (F)

3.1.3 From motoneurons activities to neurograms

In order to compare the patterns generated at the level of the CPG premotor neurons with experimental data that represent the activity of a group of motor axons, we consider a layer of motoneurons driven by these CPG premotor neurons. The activity of the two populations of motoneurons depends on their parameters and the input currents they receive (equations (10) and (11)). The global motoneuron activity generates simulated neurograms, that are compared to experimental neurograms.

Table 3 Correspondence between σ and the noise ratio in the simulations illustrated in Fig. 5

σ	0.2	0.9	1.7	2.6	4.3
noise ratio %	3	15	30	45	60

Motoneuron recruitment The curves in Fig. 6a represent the neuron number as a function of its threshold current (it also represents the number of recruited neurons as a function of the input current) for the two motoneuron populations $MN1$ and $MN2$, at both values of pH. The components of the extrinsic currents from the CPG network and the noise current are represented in Fig. 6b. All $MN1$

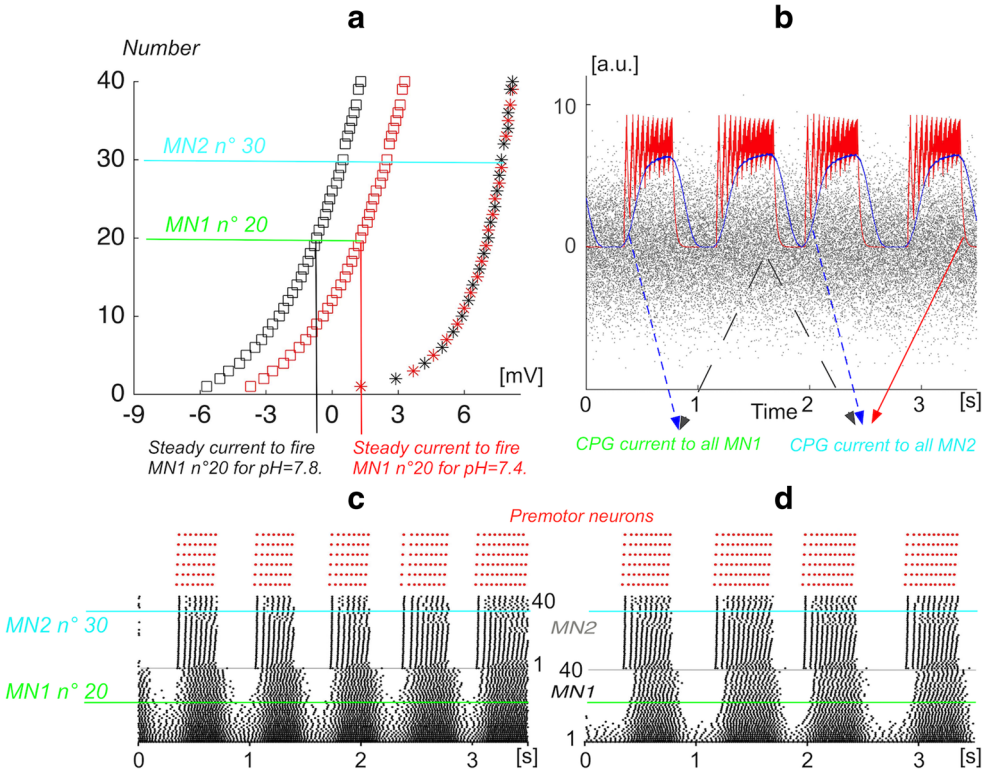

Fig. 6 Recruitment and activity patterns of motoneurons. **a** Recruitment curves of $MN1$ (square) and $MN2$ (asterisk) motoneurons at $pH = 7.8$ (black) and $pH = 7.4$ (red). Two motoneurons are marked: n°20 of the $MN1$ population in green, and n°30 of the $MN2$ population in cyan. The minimal value of the steady current to fire $MN1$ n°20 at $pH = 7.8$ is indicated, in black, idem for $pH = 7.4$ in red. **b** Time evolution during 3.5 seconds of the three components of the external current received by the $MN2$ motoneurons at $pH = 7.4$: (1) the synaptic current from the premotor neurons (red), (2) the modulation current integrating the activity of excitatory and inhibitory neurons of the CPG around the premotor neurons (blue), (3) the Gaussian noise (gray dots). All $MN2$ receive these three currents. $MN1$ neurons only receive the modulation and noise currents. **c** Raster plot of 3.5 seconds of neuronal activity at $pH = 7.8$. Six premotor neurons (red) and 80 motoneurons (black, 40 $MN1$ and 40 $MN2$) are involved. The motoneuron activity is presented as two raster plots stacked with $MN1$ below and $MN2$ above. The neurons firing first (i.e. firing at lower currents) are at the bottom of the stack for each subpopulation, and the following neurons are ranked according to their increasing recruitment current. The firing patterns of two motoneurons: $MN1$ n°20 and $MN2$ n°30 are underlined, in green and in cyan, respectively. **d** Raster plot of 3.5 seconds of premotor neuron activity and motoneuron activity at $pH = 7.4$

motoneurons receive the same modulation current and a noise current: their individual activity depends on their individual threshold. The same process applies for $MN2$ motoneurons, which also receive the premotor synaptic current. These motoneuron activities for populations $MN1$ and $MN2$ are shown in Fig. 6c and d, at $pH = 7.8$ and $pH = 7.4$ respectively. For the same simulation duration of 3.5 seconds, we observe 5 bursts at $pH = 7.8$ and only 4 bursts at $pH = 7.4$, as a direct consequence of the burst frequency decrease at the CPG premotor level, in response to the frequency increase in the chemosensitive pacemaker CH.

Simulated and experimental neurograms As described in Section 2.5, the simulated neurograms result from the weighted summation of the motoneuron membrane potential derivatives. The quasi-synchronous spiking of the $MN2$ motoneurons, mainly recruited by the 6 premotor neurons of the CPG (Fig. 6), is at the origin of the high amplitude peaks in the neurograms, and thus at the origin of the S_{10} signal intraburst oscillations. They reflect the B follower activity pattern. The asynchronous spiking of the $MN1$ motoneurons is due to the global modulation from the CPG and leads to higher neuronal activity in the middle of each burst (Fig. 6). This asynchronous activity is at the origin of the 'bump' that carries the oscillations in the simulated S_{10} signal in Fig. 7. The noise at the motoneuron level affects the burst activity and generates a few interburst spikes, which are more numerous at $pH = 7.8$ than at $pH = 7.4$. Because the $pH = 7.4$ recruitment curve is shifted towards higher values, a same noise level at both pH leads to a smaller number of recruited motoneurons at $pH = 7.4$. These features - oscillations, 'bump' and interburst activity- are similar to those observed in the experimental traces from the pre-metamorphic tadpole brainstem preparations.

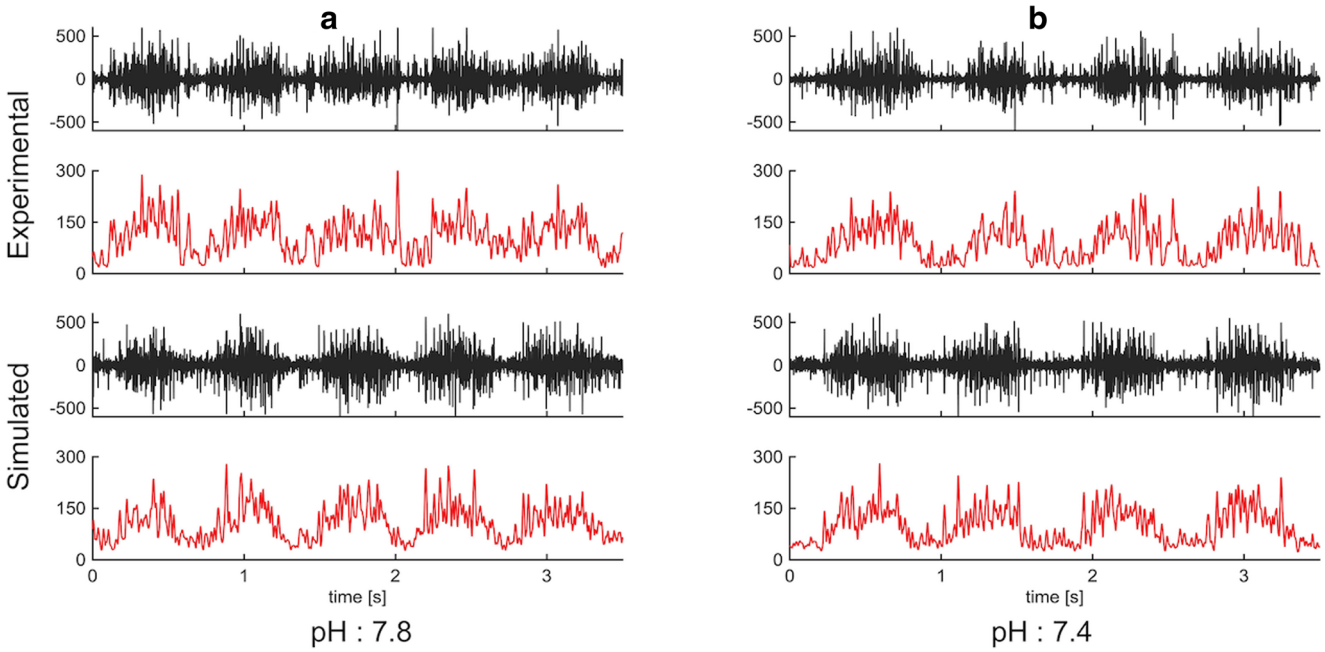

Fig. 7 Experimental and simulated traces (neurograms and S_{10} signals) in pre-metamorphic tadpoles, at $pH = 7.8$ (**a**) and $pH = 7.4$ (**b**). In both experimental and simulated neurograms (black), five buccal bursts occur at $pH = 7.8$, and only four bursts at $pH = 7.4$, in a 3.5 second period. Simulated neurograms are visually similar to the experimental neurograms. In all cases, S_{10} signals (red) show the same types of intraburst oscillations

Amplitude and frequency profiles Simulations were performed in order to get simulated neurograms corresponding to five minute recordings. Deeper insights in the comparison between simulated and experimental data are obtained by applying to the simulated neurograms the analysis tools previously applied to the experimental neurograms. Segmentation and cycle alignment by cross-correlation allows cycle maps to be built, and mean amplitude profiles to be computed (see Fig. 8a, b, c, for $pH = 7.8$ and $pH = 7.4$). All the cycle maps (experimental and simulated) reveal very similar vertical dark bands corresponding to local amplitude maxima of the S_{10} cycles, on which the maxima of the mean amplitude curves are superimposed. These maps and profiles reveal the structured oscillations of the buccal bursts.

CWT allows time-frequency maps to be built, and mean frequency profiles (or CWT spectra) to be computed. All the profiles, at both values of pH, exhibit two peaks: an LF peak around 1 Hz, and an HF peak around 21 Hz. However, the amplitude of the 1.5 Hz peak in the $pH = 7.8$ profile (blue line) is higher for the simulated data than that of the experimental data, which suggests a lower variability of the buccal cycle duration in the simulation than in the experimental data. As a consequence, a small peak at double the value of the LF (i.e, its second harmonic), appears in simulation profiles but is absent in the illustrated experimental profile (T2 in Quenet et al. 2014). Note that another experimental neurogram, also exhibits such a second harmonic at $pH = 7.8$, in relationship with a more stable corresponding LF (see T3 frequency profile: Fig. 4 in Quenet et al. 2014), i.e. the variability is less than in the T2 example. In the simulated neurograms, the variability of the buccal cycle duration is mainly due to noise in the CPG.

Simulation of suppressing the buccal activity Figure 9 shows that two configurations of the connection matrix in the CPG produce quasi-identical S_{10} signals computed from the simulated neurograms (see A2 and B2 corresponding to matrices A1 and B1, respectively). The A1 and B1 matrices represent the same connectivity but in B1 the excitatory synapses to and from L follower are significantly higher than in A1. The buccal activity is the same when simulated in either configuration. In both configurations the L follower is silent: in configuration A1, the silence of L is due to a subthreshold excitation, while in configuration B1, the silence of L relies on a balance between the excitation and inhibition it receives. This inhibition is activated, because the chain neurons are activated by the B follower. The interest of configuration B1 is that it permits possible lung burst activity: in a simulation of 300 seconds a single lung spike occurred (not shown). Experimental recordings from *Pelophylax ridibundus* brainstem preparations have shown that some pre-metamorphic preparations exhibit infrequent lung bursts (Straus et al. 2011). Such lung activity has also been observed in pre-metamorphic brainstem preparations from the *Rana Catesbaiana* tadpole

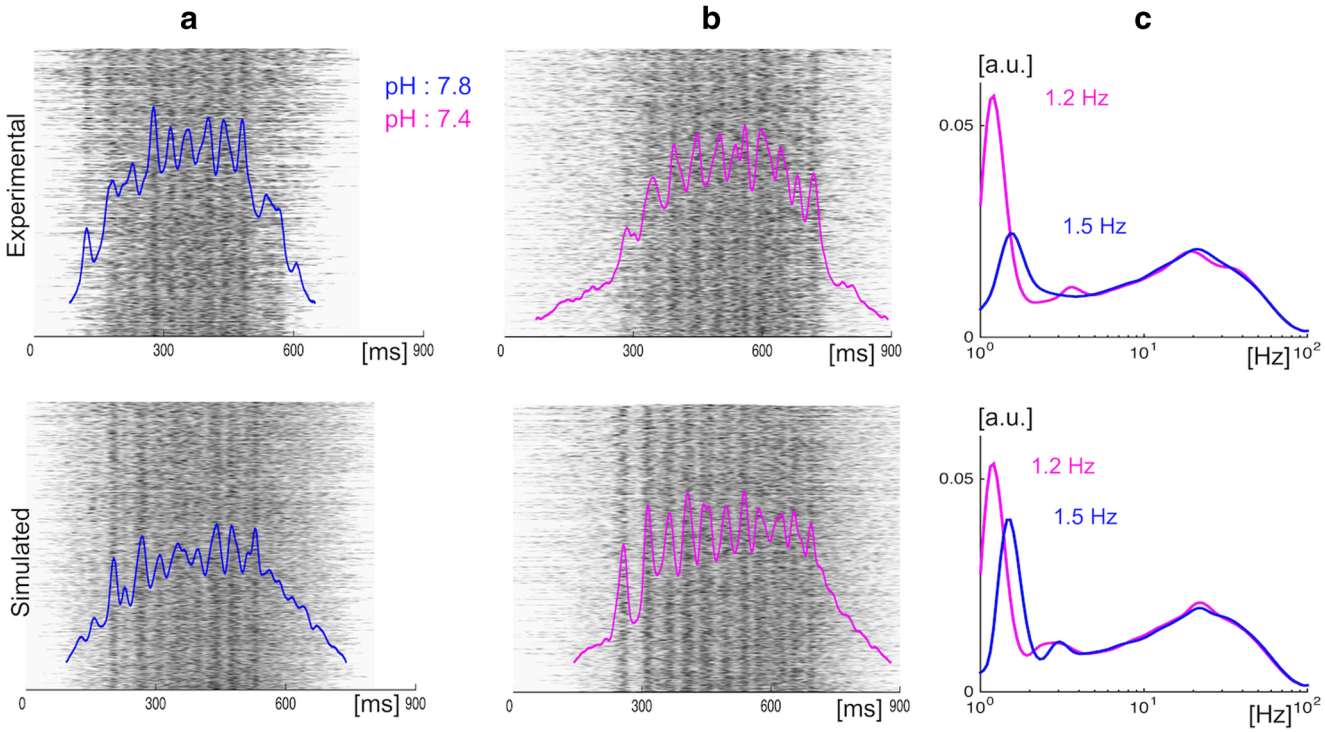

Fig. 8 Simulated and experimental amplitude profiles and frequency profiles. **a** and **b** Amplitude cycle maps and profile computed from the S_{10} simulated and experimental signals. Each cycle map is built by stacking the segmented cycles and by positioning them using cross correlation with a reference cycle; each line of the map represents one cycle whose amplitude value is coded in gray scale. An amplitude profile (blue for $pH = 7.8$ in A and magenta for $pH = 7.4$ in **b** corresponds to the mean cycle amplitude value. Upper row: experimental data; lower row: simulated data. **c** Frequency profiles (or CWT spectra) computed from the S_{10} signals, presented with a logarithmic frequency scale. A frequency profile (blue for $pH = 7.8$ and magenta for $pH = 7.4$) corresponds to the normalized mean map amplitude value for each frequency. Upper row: experimental data; lower row: simulated data

(Gdovin et al. 1999). This lung activity may occur more frequently when the buccal activity is suppressed, by synaptic blockade of the caudal part of the brainstem which contains components of the ventilatory CPG (Duchcherer et al. 2013). To test the effect of suppressing buccal activity in the model, simulations were performed using the connection matrix C1, where the *B* follower is completely disconnected from the CPG network, as well as the more 'caudal' neurons of the chain, i.e., neurons n°61 to n°71 (Fig. 9d). The corresponding S_{10} signal exhibits no buccal activity at all, but does exhibit episodic short bursts driven by the *L* follower only, which synchronizes all of the chain neurons, and in particular the premotor neurons. This premotor synchronization leads to complete motoneuron recruitment. In the model, the episodic 'lung' activity results from a supra-threshold synaptic balance at the level of the *L* follower, as is frequently the case with the excitatory connections in matrix B1 when the *B* follower is disconnected. Thus, the buccal rhythm is absent in the chain, as well as from the periodic inhibition on the *L* follower, so at the level of the neurogram, only *L* episodes are present.

3.2 Post-metamorphic stage

We hypothesize that metamorphic processes include some modifications to the neuronal properties and synaptic connections of the CPG network. At the post-metamorphic stage, both buccal CPG activity and lung activity are present, and we hypothesize that lung activity becomes more frequent given its functional importance. The lung episodic activity occurs and is visible in neurograms as shorter bursts of higher amplitude than the buccal bursts, due to the synchronization process.

3.2.1 Activity of the CPG

The CPG architecture is the same as in Fig. 2a. The post-metamorphic changes concern some neuronal properties (illustrated in Fig. 10a: the inhibitory and excitatory neurons of the chain are more responsive). They also concern the synaptic connection matrix that is based on matrix B1 (Fig. 9b): there are two new inhibitory connections from neuron n°5 and neuron n°7 to the buccal follower. In the example of CPG activity shown in Fig. 10, the values of

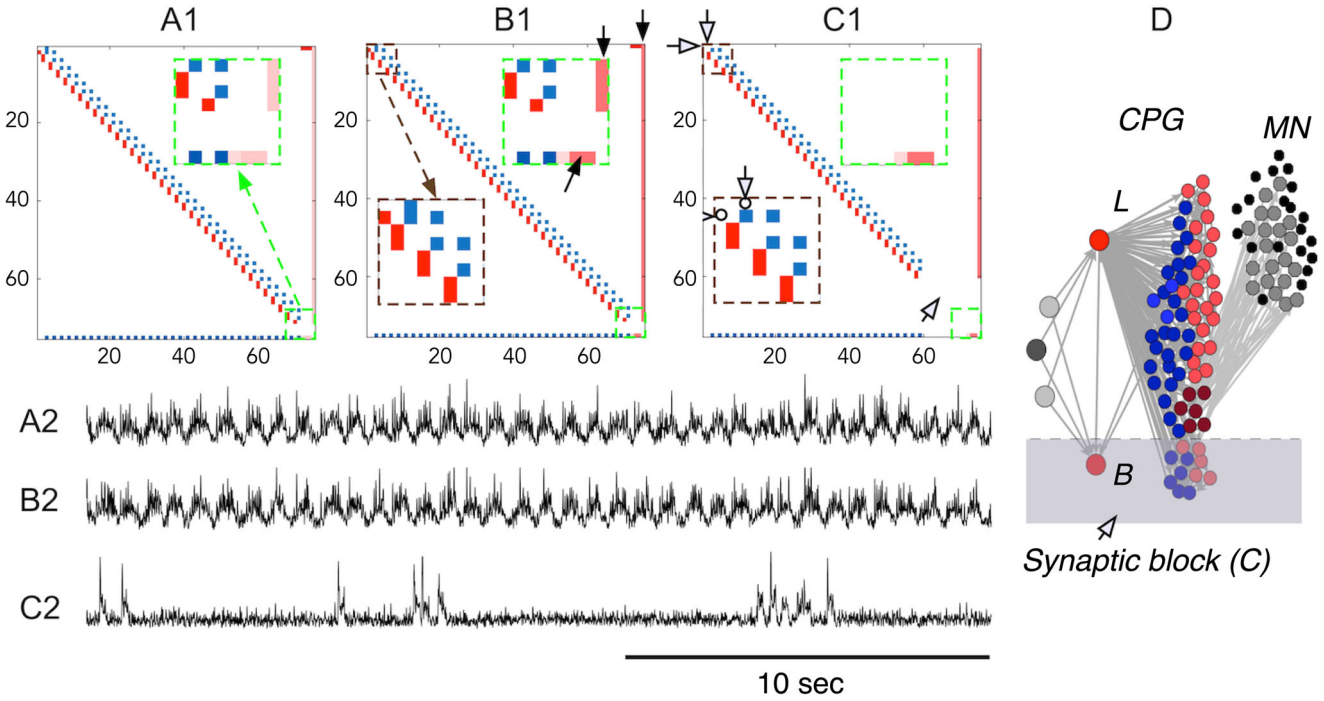

Fig. 9 Simulation of synaptic blockade of the 'caudal part' of the CPG. A1 is the same synaptic connection matrix as in Fig. 4; B1 is based on A1, but the excitatory synaptic weights from the pacemakers to L follower and from L follower to the other neurons are stronger than in A1 (see the insets surrounded by green dashed lines and brown dashed lines, which are enlarged views of small square parts on the diagonal of the matrix). S_{10} signals computed from simulated neurograms with these two CPG matrices lead to indistinguishable buccal activities as shown in A2 and B2, respectively. The connection matrix C1 is based on B1, but corresponds to a situation where the synapses of what is considered as the most caudal part of the network (including B follower and the caudal part of the chain loop) are 'blocked', i.e set to zero. This synaptic suppression is illustrated in C1 by arrows in the matrix. The simulation of the neurogram corresponding to this CPG configuration exhibits the activity illustrated by S_{10} in C2, characterized by the absence of buccal activity, and the occurrence of episodic bursts driven by the L follower, which are reminiscent of those observed experimentally (see Fig. 5 in (Duchcherer et al. 2013))

the buccal and lung frequencies are close to those measured in tadpole F2 studied by Quenet et al. (2014). As in the pre-metamorphic CPG, the buccal rhythm in the post-metamorphic CPG is generated by a quasiperiodic bursting activity of the buccal follower, whose basic frequency is, as previously, the difference between BP frequency and the chemosensitive pacemaker CH frequency.

The inhibition received by the B follower from the first three inhibitory neurons of the chain modulates the intraburst frequency and suddenly interrupts its activity at the end of each burst, when its spiking frequency is at its maximum. BP frequency is set at 34.3 Hz, and CH frequency is set at 31.1 Hz for $pH = 7.8$ and at 32.3 Hz for $pH = 7.4$. Thus, the buccal frequency appears near 3.2 Hz for $pH = 7.8$ and at 2 Hz for $pH = 7.4$ respectively, as observed in a post-metamorphic *Pelophylax ridibundus* tadpole. Mean LP frequency is set at 30.95 Hz, lower than the frequencies of CH at both values of pH, in such a way that the second effect of increasing CH frequency from 31.1 Hz for $pH = 7.8$ to 32.3 Hz for $pH = 7.4$ is an increase in the L follower spiking frequency. The mechanism of this L follower frequency increase is explained by an increase in the periodic variations of its membrane potential, as illustrated in Fig. 11.

The lung follower membrane potential (MP) exhibits a quasi-periodic complex modulation. Its lowest frequency component corresponds to the interaction between the LP and CH pacemakers, at 0.15 Hz for $pH = 7.8$. Another low frequency component of MP appears as the interaction between the BP and CH pacemakers, due to the periodic inhibitory modulation from the chain at 3.2 Hz, i.e. at the buccal frequency. The weights of the excitatory connections from the pacemakers to the L follower are set in order to obtain only a few L spikes at $pH = 7.8$ (4 L spikes during a 300 s simulation; no L spike at all in the 20 s time window illustrated in Fig. 11a). When the CH pacemaker's frequency is increased, corresponding to $pH = 7.4$, the lowest frequency component is increased. This means the MP value exceeds the spiking threshold more frequently (19 L spikes in a 300 s simulation; 1 L spike at the end of the 20 s time window illustrated in Fig. 11b).

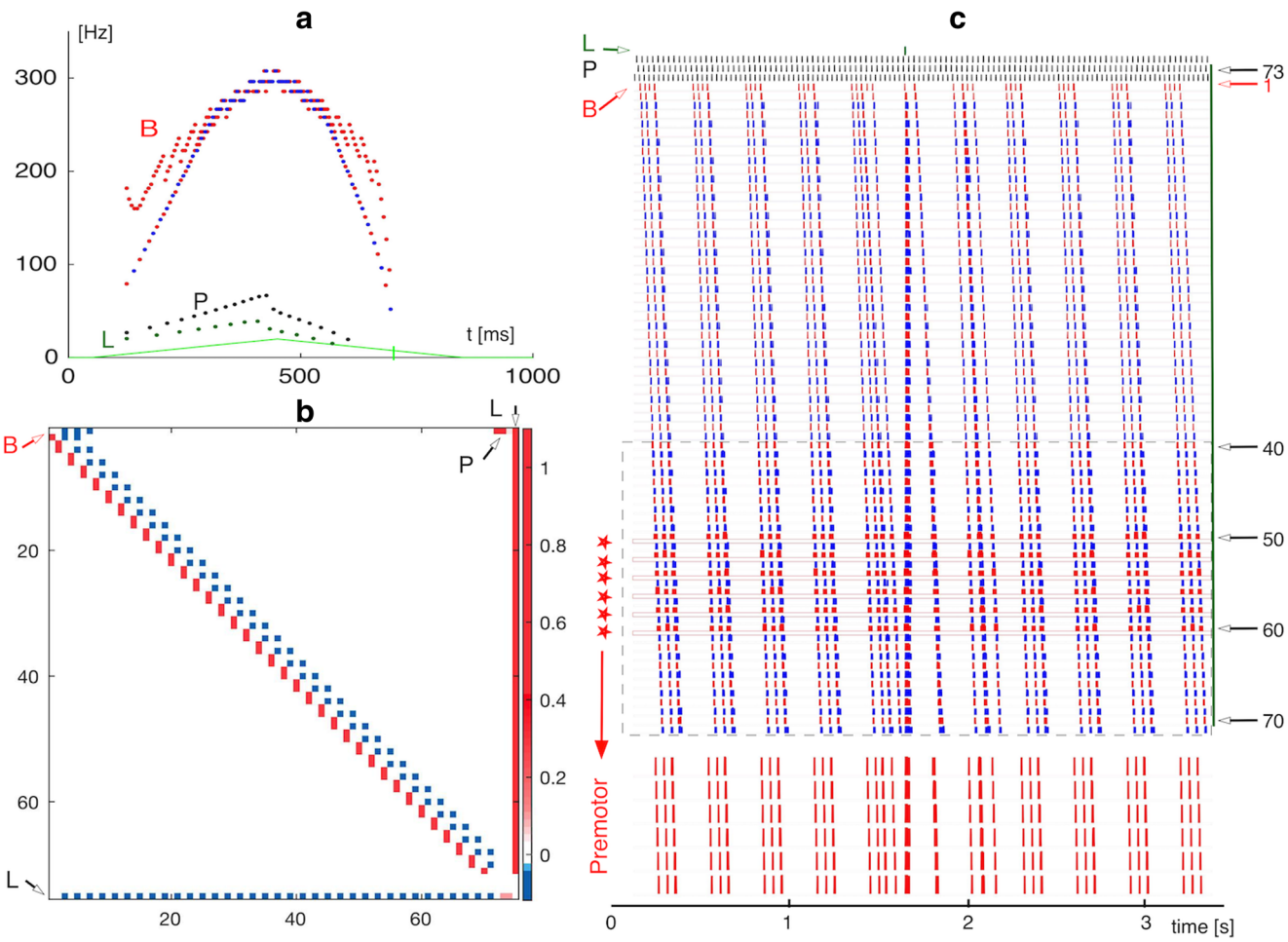

Fig. 10 Neuronal components, network connectivity and activity of the post-metamorphic ventilatory CPG. **a** Frequency up-down ramp current curves of the three types of the CPG neurons (the maximum of the double ramp current is set at a value which corresponds to an external depolarization of 20 mV for all neurons): P, for the pacemakers (black dots), B, for the buccal follower (red dots), L, for the lung follower (dark green dots) and the other excitatory (red dots) and inhibitory (blue dots) neurons of the chain. **b** Connection matrix of the CPG network. The red squares represent the excitatory connections, and the blue squares the inhibitory connections. **c** Raster plot, representing 3.5 seconds of neuronal activity for $pH = 7.8$. The six excitatory premotor neurons are indicated by an asterisk. They are surrounded by 10 preceding neurons (5 excitatory and 5 inhibitory neurons) and 10 following neurons (5 excitatory and 5 inhibitory neurons). Together they define a neuronal population (dashed rectangle in **c** that contributes to motoneuron activity through its modulation current. A scatter plot of the activity of the premotor neurons alone is reproduced below, where there is a lung follower spike synchronizing all chain neurons

3.2.2 From motoneurons activities to neurograms

The neurograms are built using the same process as for the pre-metamorphic stage. The motoneuron layer in the post-metamorphic stage comprises 100 $MN1$, 50 $MN2$ and 100 additional motoneurons of a third population, $MN3$.

Motoneuron recruitment The curves in Fig. 12a represent the neuron number as a function of its threshold current for the three motoneuron populations $MN1$, $MN2$ and $MN3$, at both values of pH. The thresholds of $MN3$ population motoneurons are higher than those of $MN1$ and $MN2$, in such a way that the $MN3$ population is recruited only when the premotor neurons fire synchronously, which occurs when L follower fires. The components of the extrinsic currents from the CPG network are represented in Fig. 12b, and are constructed as previously described for the pre-metamorphic stage. $MN1$ receives two extrinsic input currents, $I^{add}(t)$ and $I_m^{stoch}(t)$. $MN2$ and $MN3$ receive both these same two extrinsic input currents, and the synaptic current from the premotor neurons, $\sum_{j=1}^{N^{cpg}} I_j^{syn}(t)$. The motoneuron activities for the three populations are shown in Fig. 12c and d, for $pH = 7.8$ and $pH = 7.4$ respectively. For the same simulation duration of 3.5 seconds, we observe 15 buccal bursts around a lung burst at $pH = 7.8$; at $pH = 7.4$ we observe 9 buccal bursts around a lung burst. Fewer motoneurons

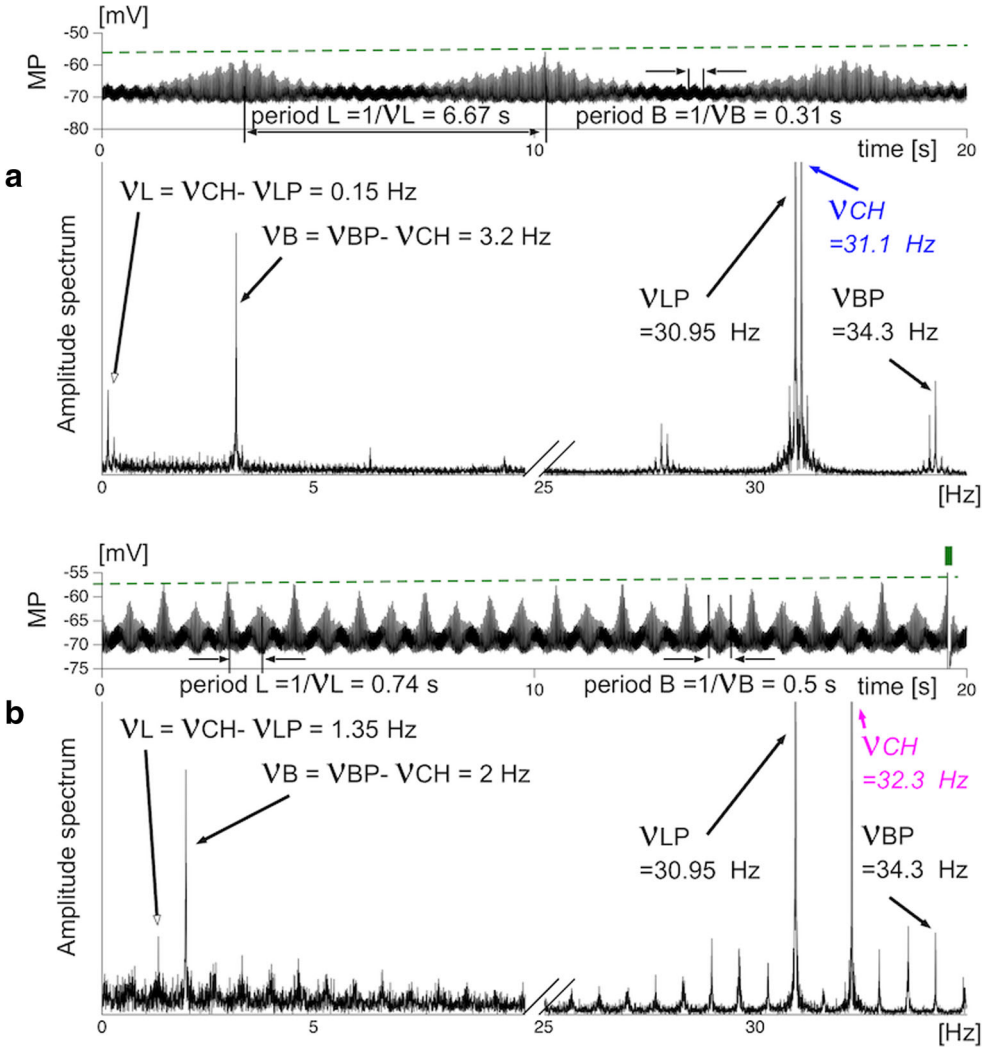

Fig. 11 Modulation of the L follower membrane potential (MP) at both values of pH. **a** Upper part: 20 seconds of MP extracted from a 300 second simulation of the post-metamorphic CPG model at $pH = 7.8$. MP exhibits periodic modulations at 0.15 Hz due to the pacemaker interaction effects: the MP is beneath the spiking threshold (green dashed line) but periodically approaches this value. Lower part: frequency spectrum obtained by Fast Fourier Transform exhibiting (1) three dominant high frequency peaks (above 25 Hz) corresponding to LP, CH (blue), and BP pacemaker frequencies and (2) two dominant low frequency peaks (below 10 Hz) resulting from their interactions, respectively between CH and LP at 0.15 Hz, and CH and BP at 3.2 Hz, i.e. the buccal frequency. The first peak at 0.15 Hz corresponds to the slow periodic modulation of MP, with a period of 6.67 s. **b** Upper part: 20 seconds of MP computed at $pH = 7.4$, with one occurrence of an L follower action potential (small green vertical bar). Lower part: frequency spectrum of MP with the three high frequency peaks of LP, CH (magenta), and BP, with a higher CH frequency than in **a**. Two low frequency peaks also result from the interactions between the pacemaker frequencies. Due to the CH frequency shift, the buccal frequency is now lower, at 2 Hz, while the lowest frequency modulating MP is now higher, at 1.35 Hz, with a corresponding period of 0.74 s. In this situation, the periodic maxima MP are more frequently near the spike threshold

are recruited in each population at $pH = 7.4$ than at $pH = 7.8$.

Simulated and experimental neurograms The buccal bursts in the post-metamorphic experimental neurograms are very different in shape from a typical buccal burst at the pre-metamorphic stage (see Fig. 13a and Fig. 7a). Furthermore, acidosis affects both the shape and amplitude of the buccal bursts. As in the pre-metamorphic case, this acidosis leads to a decreased buccal burst frequency. The experimental lung episodes appear as very short high amplitude bursts, sometimes organized as doublets (see Fig. 13b). The simulated post-metamorphic neurograms capture these features.

Time-frequency maps, frequency profiles and lung activity Figure 14 illustrates time-frequency maps computed on experimental and simulated S_{10} signals at both values of pH. At $pH = 7.8$, the black band at the bottom of the experimental and simulated maps corresponds to the LF

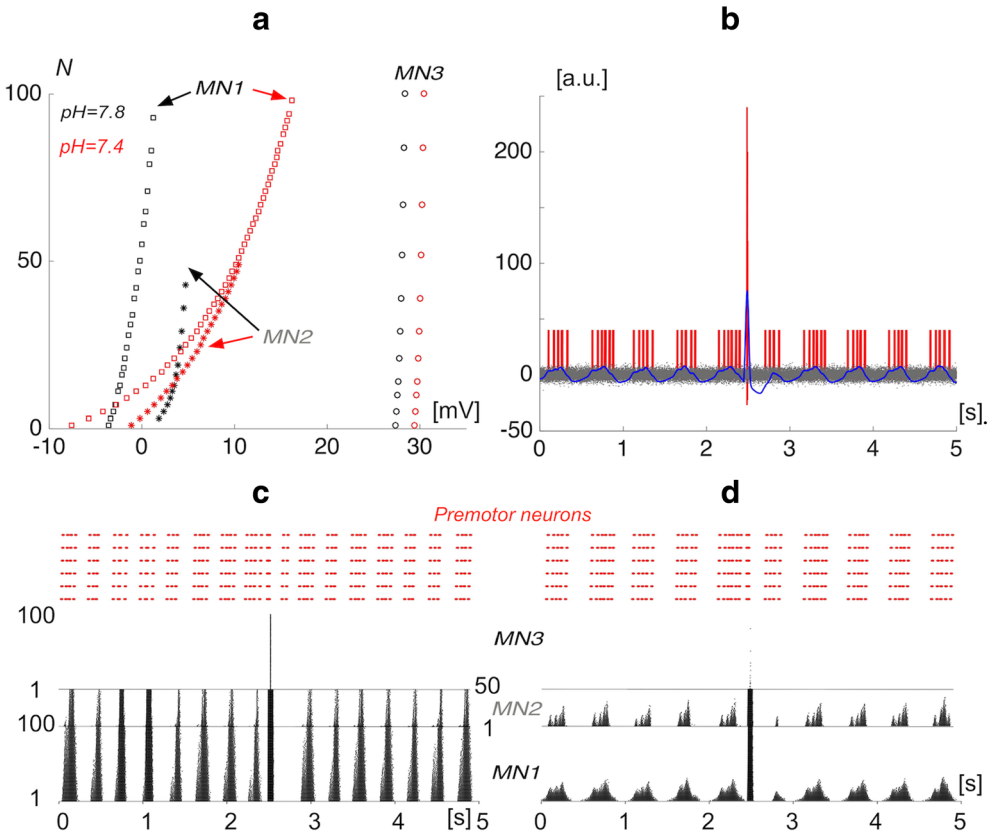

Fig. 12 Recruitment curves and activity patterns of motoneurons. **a** Recruitment curves of $MN1$ (squares), $MN2$ (asterisks) and $MN3$ (circles) motoneurons at $pH = 7.8$ (black) and $pH = 7.4$ (red). **b** Evolution of the three components of the external current received by $MN2$ and $MN3$ populations over a five second period: (1) the synaptic current from the premotor neurons (red); (2) the modulation current integrating the activity of excitatory and inhibitory neurons of the CPG around the premotor neurons (blue); (3) with Gaussian noise (gray dots). **c** Raster plot of six seconds of neuronal activity involving six premotor neurons (red) and 250 motoneurons (black, from bottom to top: 100 $MN1$, 50 $MN2$, and 100 $MN3$) at $pH = 7.8$. **d** Raster plot of five seconds of premotor neuron activity and motoneuron activity at $pH = 7.4$

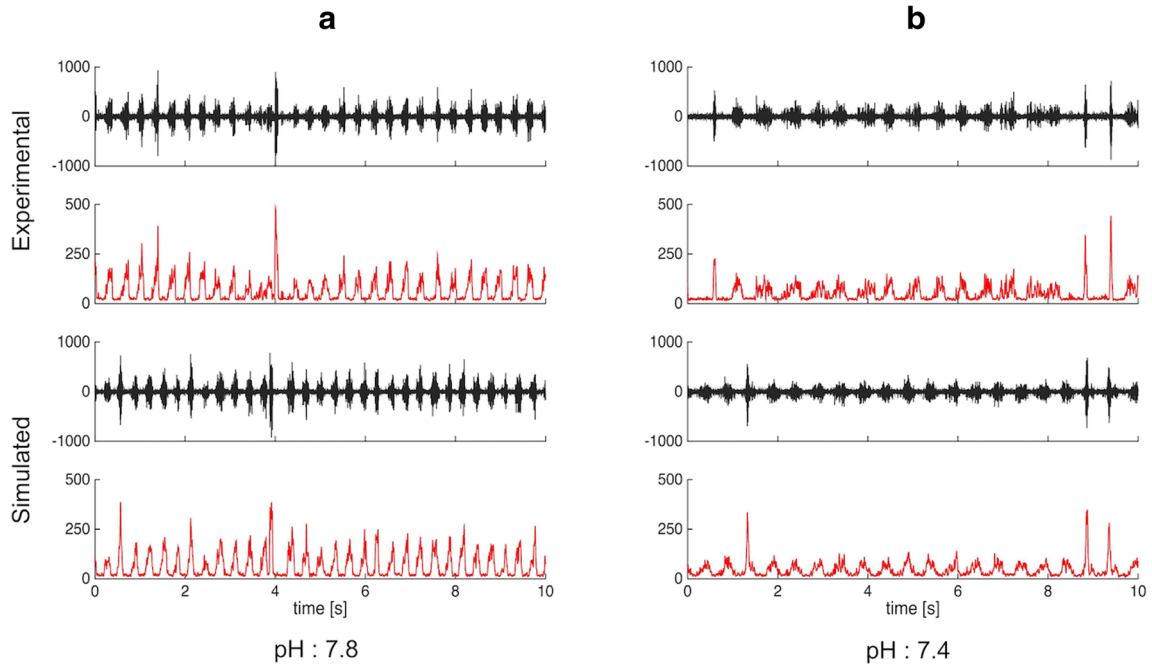

Fig. 13 Experimental and simulated traces (neurograms and S_{10} signals) in post-metamorphic tadpoles, at $pH = 7.8$ (**a**) and $pH = 7.4$ (**b**). In both experimental and simulated neurograms (black), both buccal and lung bursts are present at $pH = 7.8$, with fewer buccal bursts and more lung bursts at $pH = 7.4$ in a 10 second period, and a lower amplitude for both burst types

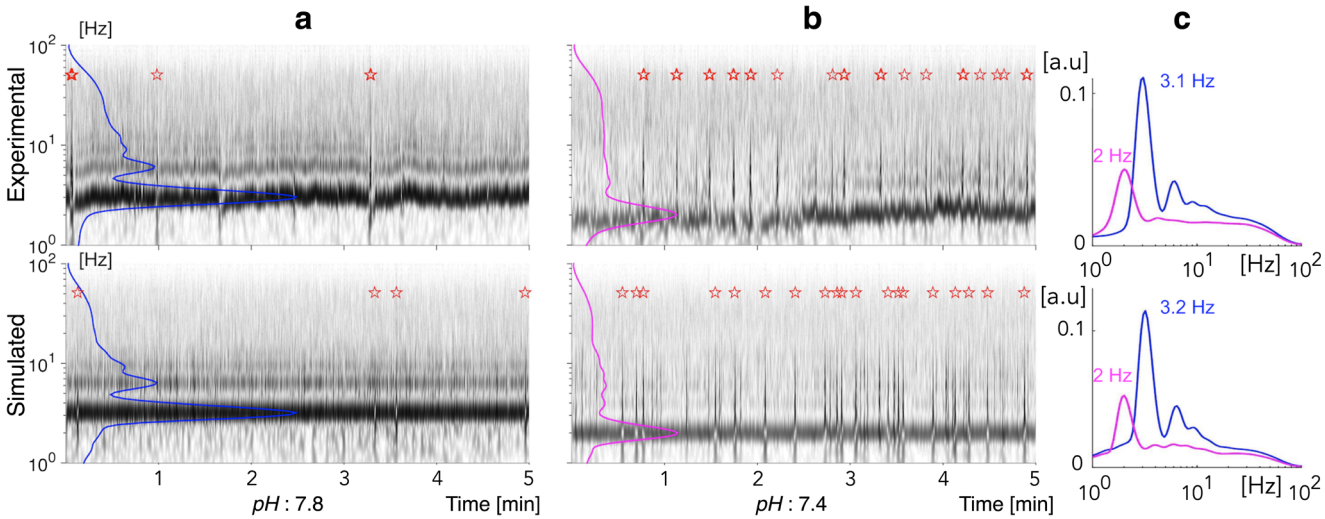

Fig. 14 Time-frequency maps and frequency profiles. The maps are computed from the S_{10} signals, and are presented with a logarithmic frequency scale. The map amplitude is coded in gray scale. The profile (blue line ($pH = 7.8$) or magenta line ($pH = 7.4$)) corresponds to the normalised mean map amplitude value for each frequency. Upper row: experimental data; lower row: simulated data. **a** $pH = 7.8$, **b** $pH = 7.4$. Each map exhibits at least one dark horizontal band at low frequency, resulting from quasi-periodic buccal activity. The maps also exhibit dark vertical striae labeled with red stars, which correspond to lung bursts. As in the experimental situation, the simulation at $pH = 7.4$ induces both a decreased buccal frequency and an increased number of episodic lung bursts. **c** Superimposed frequency profiles

buccal activity. The second dark band, above the previous one, is thinner, and appears at twice the peak frequency value in the frequency profile, and corresponds to the second harmonic of the periodic buccal activity. At $pH = 7.4$, the harmonic band is quasi-absent, and the first band shifts towards a lower frequency value (Fig. 14c). In experimental and simulated maps, the dark vertical striae correspond to lung episodes: in both cases they are about five time more frequent at $pH = 7.4$ than at $pH = 7.8$.

4 Discussion

The present ventilatory amphibian CPG model introduces two new concepts: (1) a central chemosensitivity as a pacemaker property and (2) the 'co-genesis' of two rhythms resulting from the interference between pacemakers. The CPG model we propose here generates rhythms and patterns of the ventilatory amphibian neural network, through a small core of 5 neurons and a chain of 70 neurons. This model is based on four generic principles:(1) the interactions between pacemaker neuron frequencies -these pacemakers are common inputs to the buccal follower and to the lung follower and the two follower responses are at the origin of the buccal periodic activity and of the lung episodic activity, respectively; (2) the propagation along a loop chain of the buccal follower activity; (3) the synchronisation of the chain neurons at the occurrence of each lung spike; and (4) the inhibition of the lung follower by the inhibitory neurons of the chain. The model accounts for the hypercapnia (or acidosis) effects: this chemosensitivity is mediated by one of the core pacemakers, whose spiking frequency increases with acidosis. Examples of such chemosensitive pacemakers have also been observed in rat upper medulla (Rigatto et al. 2000).

Among the available spiking neuron models for simulating networks of biologically plausible neurons (Ibarz et al. 2011; Abusnaina and Abdullah 2014), we chose Izhikevich formal neurons. This represented an efficient alternative approach to the small integration step and exhaustive equations required by the Hodgkin-Huxley model. The Izhikevich model realistically accounts for a wide range of spiking dynamics while being highly computationally efficient. A large panel of neuronal types is straightforward to implement through the four parameters a, b, c, and d of equations (1) and (2). Simulations are performed that exhibit the neuronal activity induced by the CPG architecture, and, secondarily, show the dynamic recruitment of the motoneuron populations. The representative neurograms are built from this motoneuron spiking, and compared to the experimental ones. The patterning of the buccal neurograms bursts includes the intra-burst HF structured at the level of the B follower. Moreover, at each step of the activity transmission along the chain, this intra-burst spiking pattern is slightly modified along the chain, obtaining increasing regularity. The motoneuron recruitment contributes to the final patterning.

Each simulation aims at reproducing the main characteristics of specific experimental situations at pre- or post-metamorphic stage, with given sets of parameters. For

other experimental examples, this set may be modified. However, different sets of parameters may lead to equivalent simulations, because the key dynamic features result from the generic principles. With these principles, the CPG model dynamics was robust against the synaptic noise that was added to all neuron currents. The primary source of synaptic noise comes from background synaptic input activities. We suppose that the CPG network is embedded in a global network and that the synaptic noise results from input action potentials carried by a large number of afferent inputs that can be modeled as a high-rate Poisson process, well-approximated by a Gaussian white-noise source (Brunel et al. 2001).

The CPG neuron dynamic pattern, when driven by the buccal follower, exhibits two frequencies, whose value and stability have been studied as functions of the synaptic noise. The core 'pacemaker interaction' that drives the buccal follower appears to be a basic mechanism for robust rhythm generation. Beyond the 5 neuron network of this core, there is the inhibitory feedback from the chain inhibitory neurons which embed the follower neurons in a recurrent network that contributes to dynamic stability. The inhibitory feedback from the chain to the lung follower contributes to the regulation of the lung spiking frequency by the buccal activity, which is also driven by pacemaker interaction. Thus inhibition plays a major role, as supported by several studies (Galante et al. 1996; Straus et al. 2000; Straus et al. 2000). In our simulations, different values of synaptic weights were considered. Though the excitatory/inhibitory balance of these was set at several levels, as shown, for instance in Fig. 9a1 and b1 matrix connections, these led to the same buccal rhythm, without or with a possible lung spike occurrence. These different configurations of the excitatory/inhibitory balance could correspond to different maturation stages, beginning with weak excitatory and inhibitory weights (Fig. 9a1) and progressing to higher values (Fig. 9b1) when lung activity arises. Though buccal activity continues to be present, there is a progression to the post-metamorphic situation, where lung activity becomes functionally dominant. These two respiratory modes, buccal and lung, coexist at the late pre-metamorphic stage, and, after metamorphosis, the lung mode becomes predominant. This situation presents analogies with the salamander locomotor CPG, with its two modes, swimming and walking. Several versions of this locomotor CPG model, built with different types of neural units (Ijspeert 2001; Ijspeert et al. 2007; Knusel et al. 2013) involve a network whose architecture includes bilateral symmetric oscillator chains, ensuring a rostro-caudal traveling wave at the axis level for the swimming mode, and four coordinate units driving the limbs and synchronising parts of the chains, ensuring a stationary wave which leads to the walking mode. Each lateral chain of this salamander locomotor model is reminiscent of the loop chain of our ventilatory model, with the rostro-caudal propagation of the buccal rhythm, and each synchronising unit of the salamander locomotor model is reminiscent of our synchronising lung follower leading to the lung episodes. The pacemaker mean frequency values were set in order to produce LF and HF buccal frequencies observed in two chosen pre- and post-metamorphic *Pelophylax ridibundus* tadpoles, as well as the post-metamorphic lung frequencies, at $pH = 7.8$ and at $pH = 7.4$. The CPG model reproduces both the buccal frequency decrease and the lung frequency increase observed experimentally as the pH falls from 7.8 to 7.4, i. e. when there is an increase in chemosensitive pacemaker frequency (ν_{CH}). This results from the fact that ν_{CH} is set between the lung pacemaker frequency (ν_{LP}), and the buccal pacemaker frequency (ν_{BP}): when ν_{CH} increases in the interval $[\nu_{LP}, \nu_{BP}]$, the lung membrane potential frequency increases and LF decreases. Experimental data from neurograms recorded in brainstem preparations of *Lithobates catesbeianus* tadpoles show a systematic increase in lung frequency with hypercapnia but that the gill/buccal frequency may either decrease or increase (Taylor et al. 2003; Torgerson et al. 1997). A decrease may be explained by the same scheme described above for *Pelophylax ridibundus*, while an increase may be explained by another relative value of the pacemaker frequencies where ν_{CH} is higher than ν_{LP} and also higher than ν_{BP} at both values of pH. Note that the frequency range of the chemoreceptor pacemaker can be enlarged, since the interactions considered here between the fundamental frequency ν_{LP} (or ν_{BP}) and the fundamental frequency ν_{CH} are also possible with harmonics of ν_{CH}. These generic features of our CPG model suggest that it may be able to account for different experimental data from other amphibians, in particular *Lithobates catesbeianus*.

Galante et al. (1996) suggested that pacemakers sustain mechanisms for gill and lung ventilation in amphibians. Similarly, in experiments with *in vitro* preparations of neonatal rats, it has been shown that pacemakers are an important component of respiratory rhythmogenesis in mammals (Feldman and Smith 1989; Smith et al. 1991). Inhibition is another common feature of the two systems. For instance, in amphibian tadpoles brainstem preparations, inhibition has a crucial role in silencing lung activity (Duchcherer et al. 2013). In neonate mammals, fictive lung ventilation not only persists in the absence of extracellular Cl-ions, but the lung burst duration increases indicating comparable roles of inhibition in both systems (Feldman and Smith 1989).

From an anatomical point of view, analogies between amphibians and mammals are supported by the rhombomeric localization of the neural networks generating rhythmic behaviors (Kinkead 2009; Klingler and Hedrick

2013). In mammals, this segmental configuration appears to be transient and reconfigured during development to produce coordinated and effective movements (Kinkead 2009). It was also suggested that each major group of respiratory neurons was connected to its own rhythm generator, that may be coupled to ensure coordinated motor activity (Champagnat and Fortin 1997). Such configurations have a similarity with the ventilatory network in amphibians where the buccal oscillator critically interacts with the lung generator, in particular through indirect inhibition, even if this type of oscillator interaction is more complex in mammals (Baghdadwala et al. 2016).

Further comparison studies of possible rhythmogenic areas in frogs and mammals are certainly warranted, as presumably developmental mechanisms have been preserved during the course of evolution. Future amphibian and mammalian models should encompass the ability to evolve from one model to other, on both phylogenetic and ontogenetic grounds.

Acknowledgments We thank Jeremy Cabessa for his critical reading of the paper and Douglas Carnall for his help with English style.

Compliance with Ethical Standards

Conflict of interests The authors declare that they have no conflict of interest.

References

Abusnaina, A.A., & Abdullah, R. (2014). Spiking neuron models: a review. *JDCTA*, *8*(3), 14–21.

Anastassiou, C.A., Perin, R., Buzsaki, G., Markram, H., Koch, C. (2015). Cell type- and activity-dependent extracellular correlates of intracellular spiking. *Journal of Neurophysiology*, *114*(1), 608–23.

Anderson, T.M., & Ramirez, J.M. (2017). Respiratory rhythm generation: triple oscillator hypothesis. *F1000Res*, *6*, 139.

Baghdadwala, M.I., Duchcherer, M., Trask, W.M., Gray, P.A., Wilson, R.J.A. (2016). Diving into the mammalian swamp of respiratory rhythm generation with the bullfrog. *Respiratory Physiology & Neurobiology*, *224*, 37–51.

Ballantyne, D., & Scheid, P. (2000). Mammalian brainstem chemosensitive neurones: linking them to respiration in vitro. *The Journal of Physiology*, *525*(3), 567–77.

Bose, A., Lewis, T., Wilson, R. (2005). Two-oscillator model of ventilatory rhythmogenesis in the frog. *Neurocomputating*, *65-66*, 751–777.

Brunel, N., Chance, F.S., Fourcaud, N., Abbott, L.F. (2001). Effects of synaptic noise and filtering on the frequency response of spiking neurons. *Physical Review Letters*, *5 86*(10), 2186–9.

Burggren, W.W., & West, N.H. (1982). Changing respiratory importance of gills, lungs and skin during metamorphosis in the bullfrog Rana catesbeiana. *Respiration Physiology*, *47*(2), 151–64.

Burggren, W., & Doyle, M. (1986). Ontogeny of regulation of gill and lung ventilation in the bullfrog, Rana catesbeiana. *Respiration Physiology*, *66*, 279–291.

Carroll, M.S., & Ramirez, J.M. (2013). Cycle-by-cycle assembly of respiratory network activity is dynamic and stochastic. *Journal of Neurophysiology*, *109*(2), 296–305.

Champagnat, J.J., & Fortin, G. (1997). Primordial respiratory-like rhythm generation in the vertebrate embryo. *Trends in Neurosciences*, *20*(3), 119–124.

Diekman, C.O., Thomas, P.J., Wilson, C.G. (2017). Eupnea, tachypnea, and autoresuscitation in a closed-loop respiratory control model. *Journal of Neurophysiology*, *118.4*, 2194–2215.

Duchcherer, M., Baghdadwala, M.I., Paramonov, J., Wilson, R.J. (2013). Localization of essential rhombomeres for respiratory rhythm generation in bullfrog tadpoles using a binary search algorithm: Rhombomere 7 is essential for the gill rhythm and suppresses lung bursts before metamorphosis. *Developmental Neurobiology*, *73*(12), 888–98.

Feldman, J.L., & Smith, J.C. (1989). Cellular mechanisms underlying modulation of breathing pattern in mammals. *Annals of the New York Academy of Sciences*, *563*, 114–130.

Feldman, J.L., & Del Negro, C.A. (2006). Looking for inspiration: New perspectives on respiratory rhythm. *Nature Reviews Neuroscience*, *7*, 232–242.

Galante, R.J., Kubin, L., Fishman, A.P., Pack, A.I. (1996). Role of chloride-mediated inhibition in respiratory rhythmogenesis in an in vitro brainstem of tadpole, Rana catesbeiana. *Journal of Physiology*, *492*, 545–558.

Gargaglioni, L.H., & Milsom, W.K. (2007). Control of breathing in anuran amphibians. *Comparative Biochemistry and Physiology, Part A: Molecular & Integrative Physiology*, *147*(3), 665–84.

Gdovin, M.J., Torgerson, C.S., Remmers, J.E. (1998). Neurorespiratory pattern of gill and lung ventilation in the decerebrate spontaneously breathing tadpole. *Respiration Physiology*, *113*, 135–146.

Gdovin, M.J., Torgerson, C.S., Remmers, J.E. (1999). The fictively breathing tadpole brainstem preparation as a model for the development of respiratory pattern generation and central chemoreception. *Comparative Biochemistry and Physiology Part A: Molecular & Integrative Physiology*, *124*, 275–286.

Guerrier, C., Hayes, J.A., Fortin, G., Holcman, D. (2015). Robust network oscillations during mammalian respiratory rhythm generation driven by synaptic dynamics. *Proceedings of the National Academy of Sciences of the United States of America*, *112*(31), 9728–9733.

Horcholle-Bossavit, G., & Quenet, B. (2009). Neural model of frog ventilatory rhythmogenesis. *Biosystems*, *97*, 35–43.

Ibarz, B., Casado, J.M., Sanjuan, M.A.F. (2011). Map-based models in neuronal dynamics. *Physics Reports*, *501*, 1–74.

Ijspeert, A.J. (2001). A connectionist central pattern generator for the aquatic and terrestrial gaits of a simulated salamander. *Biological Cybernetics*, *84*(5), 331–48.

Ijspeert, A.J., Crespi, A., Ryczko, D., Cabelguen, J.M. (2007). From swimming to walking with a salamander robot driven by a spinal cord model. *Science*, *315*(5817), 1416–20.

Izhikevich, E.M. (2003). Simple model of spiking neurons. *IEEE Transactions on Neural Networks*, *14*, 1569–1572.

Izhikevich, E.M. (2004). Which model to use for cortical spiking neurons? *IEEE Transactions on Neural Networks*, *15*, 1063–1070.

Kinkead, R. (2009). Phylogenetic trends in respiratory rhythmogenesis: insights from ectothermic vertebrates. *Respiratory Physiology & Neurobiology*, *168*(1-2), 39–48.

Klingler, M.J., & Hedrick, M.S. (2013). Evidence for rhombomeric organization of multiple respiratory oscillators in the bullfrog brainstem. *Respiratory Physiology & Neurobiology*, *186*(1), 7–15.

Knusel, J., Bicanski, A., Ryczko, D., Cabelguen, J.M., Ijspeert, A.J. (2013). A salamander's flexible spinal network for locomotion,

modeled at two levels of abstraction. *Integrative and Comparative Biology*, *53*(2), 269–82.

Lal, A., Oku, Y., Someya, H., Miwakeichi, F., Tamura, Y. (2016). Emergent network topology within the respiratory rhythm-generating kernel evolved in silico. *PLoS One*, *11*(5), 1–32.

McLean, H.A., Kimura, N., Kogo, N., Perry, S.F., Remmers, J.E. (1995). Fictive respiratory rhythm in the isolated brainstem of frogs. *Journal of Comparative Physiology A*, *176*, 703–713.

Molkov, Y.I., Rubin, J.E., Rybak, I.A., Smith, J.C. (2017). Computational models of the neural control of breathing. *Wiley Interdisciplinary Reviews: Systems Biology and Medicine*, *9*(2), 1–22.

Oku, Y., Kimurab, N., Masumiyaa, H., Okadac, Y. (2008). Spatiotemporal organization of frog respiratory neurons visualized on the ventral medullary surface. *Respiratory Physiology & Neurobiology*, *161*, 281–290.

Onimaru, H., Ballanyi, K., Homma, I. (2003). Contribution of Ca2+-dependent conductances to membrane potential fluctuations of medullary respiratory neurons of newborn rats in vitro. *The Journal of Physiology (London)*, *552*, 727–741.

Perkel, D.H., Schulman, J.H., Bullock, T.H., Moore, G.P., Segundo, J.P. (1964). Pacemaker neurons: effects of regularly spaced synaptic input. *Science*, *145*(3627), 61–3.

Plonsey, R. (1977). Action potential sources and their volume conductor fields. *Proceedings of the IEEE*, *65*, 601–611.

Putnam, R.W., Filosa, J.A., Ritucci, N.A. (2004). Cellular mechanisms involved in CO_2 and acid signaling in chemosensitive neurons. *American Journal of Physiology - Cellular Physiology*, *287*, C1493–C1526.

Quenet, B., Straus, C., Fiamma, M.N., Rivals, I., Similowski, T., Horcholle-Bossavit, G. (2014). New insights in gill/buccal rhythm spiking activity and CO_2 sensitivity in pre- and post-metamorphic tadpoles Pelophylax ridibundus. *Respiratory Physiology & Neurobiology*, *191*, 26–37.

Rigatto, H., Rehan, V., Lemke, R.P., Idiong, N., Hussain, A., Cates, D. (2000). Respiratory pacemaker cells responsive to CO_2 in the upper medulla: dose response and effects of mediators. *Pediatric Pulmonology*, *30*(5), 359–67.

Roth, A., & Van Rossum, R.C.W. (2009). *Computation Modeling Methods for Neuroscientists*. Cambridge: MIT Press.

Rubin, J.E., Bacak, B.J., Molkov, Y.I., Shevtsova, N.A., Smith, J.C., Rybak, I.A. (2011). Interacting oscillations in neural control of breathing: modeling and qualitative analysis. *Journal of Computational Neuroscience*, *30*(3), 607–32.

Sakakibara, Y. (1984). The pattern of respiratory nerve activity in the bullfrog. *The Japanese Journal of Physiology*, *34*, 269–282.

Sakakibara, Y. (1984). Trigeminal nerve activity and buccal pressure as an index of total inspiratory activity in the bullfrog. *Japanese Journal of Physiology*, *34*, 827–838.

Santin, J.M., & Hartzler, L.K. (2013). Respiratory signaling of locus coeruleus neurons during hypercapnic acidosis in the bullfrog, Lithobates catesbeianus. *Respiratory Physiology & Neurobiology*, *185*(3), 553–6.

Smith, J.C., Ellenberger, H.H., Ballanyi, K., Richter, D.W., Feldman, J.L. (1991). Pre-boktzinger complex: a brainstem region that may generate respiratory rhythm in mammals. *Science*, *254*, 726–729.

Straus, C., Wilson, R.J.A., Remmers, J.E. (2000). Developmental disinhibition: turning off inhibition turns on breathing in vertebrates. *Journal of Neurobiology*, *45*, 75–83.

Straus, C., Wilson, R.J.A., Tezenas du Montcel, S., Remmers, J.E. (2000). Baclofen eliminates cluster lung breathing of the tadpole brainstem, in vitro. *Neuroscience Letters*, *292*, 13–16.

Straus, C., Samara, Z., Fiamma, M.N., Bautin, N., Ranohavimparany, A., Le Coz, P., Golmard, J.L., Darré, P., Zelter, M., Poon, C.S., Similowski, T. (2011). Effects of maturation and acidosis on the chaos-like complexity of the neural respiratory output in the isolated brainstem of the tadpole, Rana esculenta. *American Journal of Physiology. Regulatory, Integrative and Comparative Physiology*, *300*(5), 1163–74.

Sundin, L., Burleson, M.L., Sanchez, A.P., Amin-Naves, J., Kinkead, R., Gargaglioni, L.H., Hartzler, L.K., Wiemann, M., Kumar, P., Glass, M.L. (2007). Respiratory chemoreceptor function in vertebrates comparative and evolutionary aspects. *Integrative and Comparative Biology*, *47*(4), 592–600.

Taylor, B.E., Harris, M.B., Coates, E.L., Gdovin, M.J., Leiter, J.C. (2003). Central CO_2 chemoreception in developing bullfrogs: anomalous response to acetazolamide. *Journal of Applied Physiology*, *94*, 1204–12.

Torgerson, C.S., Gdovin, M.J., Remmers, J.E. (1997). The ontogeny of central chemoreception during fictive gill and lung ventilation of an in vitro brainstem preparation of Rana catesbeiana. *The Journal of Experimental Biology*, *299*, 2063–2072.

Vasilakos, K., Wilson, R.J., Kimura, N., Remmers, J.E. (2004). Ancient gill and lung oscillators may generate the respiratory rhythm of frogs and rats. *Journal of Neurobiology*, *62*, 369–385.

Vasilakos, K., Kimura, N., Wilson, R.J., Remmers, J.E. (2006). Lung and buccal ventilation in the frog: uncoupling coupled oscillators. *Physiological and Biochemical Zoology*, *79*(6), 1010–8.

Vinaya, M., & Ignatius, R.P. (2018). Effect of lévy noise on the networks of Izhikevich neurons. *Nonlinear Dynamics*, *94*, 1133–1150.

Wilson, R.J.A., Straus, C., Remmers, J.E. (1999). Efficacy of a low volume recirculating superfusion chamber for long term administration of expensive drugs and dyes. *Journal of Neuroscience Methods*, *87*, 175–184.

Wittmeier, S., Song, G., Duffin, J., Poon, C.S. (2008). Pacemakers handshake synchronization mechanism of mammalian respiratory rhythmogenesis. *Proceedings of the National Academy of Sciences of the United States of America*, *105*(46), 18000–5.